THESIS FOR THE DEGREE OF DOCTOR OF PHILOSOPHY

Unsupervised Segmentation of Head Tissues from Multi-Modal Magnetic Resonance Images: With Application to EEG Source Localization and Stroke Detection

QAISER MAHMOOD

CHALMERS

Department of Signals and Systems
CHALMERS UNIVERSITY OF TECHNOLOGY
Gothenburg, Sweden 2016

Unsupervised Segmentation of Head Tissues from Multi-Modal Magnetic Resonance Images: With Application to EEG Source Localization and Stroke Detection
QAISER MAHMOOD

ISBN 978-91-7597-339-5

Doktorsavhandlingar vid Chalmers Tekniska Högskola
Ny serie nr 4020
ISSN 0346-718X

Department of Signals and Systems
Imaging and Image Analysis Group
Chalmers University of Technology
SE-412 96 Gothenburg, Sweden
Phone: +46 (0)31 772 1583
Fax: +46 (0)31 772 1725
E-mail: qaiserm@chalmers.se

Printed by Chalmers Reproservice
Gothenburg, Sweden, 2016

TO MY BELOVED PARENTS AND ZOHRA

Abstract

The automated segmentation or labeling of individual tissues in magnetic resonance (MR) images of the human head is an essential first step in several biomedical applications. The resulting segmentation yields a patient-specific labeling of individual tissues that can be used to quantitatively characterize these tissues (e.g. in the study of Alzheimers disease and multiple sclerosis) or to assign individual dielectric properties for patient-specific electromagnetic simulations (e.g. in applications such as electroencephalography source localization in epilepsy patients and microwave imaging for stroke detection). Automated and accurate segmentation of MR images is a challenging task because of the complexity and variability of the underlying anatomy and the noise and the bias field (spatial intensity inhomogeneities). Consequently, manual segmentation, including both interactive segmentation and manual correction, is largely used in clinical research. However, it is time consuming, subjective, tedious, and labor-intensive. This thesis presents new segmentation methods for both the brain and whole-head that are both automatic and accurate. It also presents empirical evaluations of these methods both directly in terms of segmentation accuracy and indirectly in terms of efficacy in electroencephalography (EEG) source localization and stroke detection. The evaluations were performed using both synthetic and real MRI data. This thesis makes four distinct contributions. The first is a novel unsupervised segmentation framework for segmenting MR images of the brain into three tissue types: white matter, gray matter and cerebrospinal fluid. It is a combination of Bayesian-based adaptive mean shift, incorporating an *a priori* tissue label probability maps, and the fuzzy c-means algorithm. The experimental results —based on both synthetic T1-weighted MR images for different noise levels and spatial intensity inhomogeneity levels, and real T1-weighted MR images —demonstrate its robustness and that it has a higher degree of segmentation accuracy than existing methods. The second is a novel automated unsupervised whole-head segmentation method for the purpose of constructing a patient-specific dielectric or biomechanical head model. The method is based on a hierarchical segmentation approach incorporating Bayesian-based adaptive mean shift. The experimental results demonstrate the efficacy of the proposed method, its robustness to noise and the bias field, and that it has a higher degree of segmentation accuracy than existing methods. The third is an evaluation of the proposed whole-head segmentation method in the context of EEG source localization. The experimental results show that the proposed method yields improved localization accuracy over the commonly used method for constructing a realistic head conductivity model for EEG source localization. The fourth is an evaluation of several existing unsupervised segmentation methods including the proposed whole-head segmentation method in the context of stroke detection using a microwave imaging system. The experimental results show that the proposed method has higher image reconstruction accuracy for intracerebral hemorrhage compared to the existing methods. The results also suggest that accurate automated segmentation can be used as a surrogate for manual segmentation to obtain accurate image reconstruction of an intracerebral hemorrhage and can assist in real time stroke detection.
Keywords: Image segmentation, magnetic resonance, brain, EEG source localization, stroke, reconstruction

Preface

This thesis is in partial fulfillment of the requirements for the degree of Doctor of Philosophy at Chalmers University of Technology, Gothenburg, Sweden.

The work herein was jointly undertaken in the Imaging and Image Analysis Group within the Department of Signals and Systems at Chalmers University of Technology, and MedTech West located at Sahlgrenska University Hospital (both in Gothenburg, Sweden) between September 2010 and December 2015. It was performed under the joint supervision of Professor Mikael Persson, Dr. Artur Chodorowski and Associate Prof. Andrew Mehnert. Prof. Persson also acts as examiner of the thesis.

This work has been supported in parts by the Chalmers University of Technology and the Higher Education Commission (HEC) of Pakistan. Some of the MRI data in this thesis was acquired by the Department of Clinical Neurophysiology, Sahlgrenska University Hospital, Gothenburg, Sweden.

List of Publications

This thesis is based on the work contained in the following papers:

Paper A
Qaiser Mahmood, Artur Chodorowski, Andrew Mehnert, Mikael Persson, "A Novel Bayesian Approach to Adaptive Mean Shift Segmentation of Brain Images", *Proceedings of IEEE International Conference on Computer Based Medical Systems (CBMS)*, pp. 1-6, Rome, Italy, 20th-22nd June, 2012.

Paper B
Qaiser Mahmood, Artur Chodorowski, Mikael Persson, "Automated MRI Brain Tissue Segmentation based on Mean Shift and Fuzzy *C*-Means using *a Priori* Tissue Probability Maps", *Innovation and Research in BioMedical Engineering (IRBM)*, pp.185-196, 2015.

Paper C
Yazdan Shirvany, Antonio R. Porras, Koushyar Kowkabzadeh, **Qaiser Mahmood**, Hoi-Shun Lui, Mikael Persson, "Investigation of Brain Tissue Segmentation Error and its Effect on EEG Source Localization", *Proceedings of International Conference of the IEEE Engineering in Medicine and Biology Society (EMBC)*, pp. 1522-1525, San Diego, USA, 22nd Aug.-1st Sep., 2012.

Paper D
Yazdan Shirvany, **Qaiser Mahmood**, Fredrik Edelvik, Stefan Jakobsson, Anders Hedström, Mikael Persson, "Particle Swarm Optimization Applied to EEG Source Localization of Somatosensory Evoked Potentials", *IEEE Transactions on Neural Systems and Rehabilitation Engineering*, pp. 11- 20, 2013.

Paper E
Qaiser Mahmood, Artur Chodorowski, Andrew Mehnert, Johanna Gellermann, Mikael Persson, "Unsupervised Segmentation of Head Tissues from Multi-modal MR Images for EEG Source Localization", *Journal of Digital Imaging (JDI)*, pp. 1-16, 2014, DOI:10.1007/s10278-014-9752-6.

Paper F
Qaiser Mahmood, Shaochuan Li, Andreas Fhager, Stefan Candefjord, Artur Chodorowski, Andrew Mehnert, Mikael Persson, "A Comparative Study of Automated Segmentation Methods for Use in a Microwave Tomography System for Imaging Intracerebral Hemorrhage in Stroke Patients", *Journal of Electromagnetic Analysis and Applications (JEMAA)*, Online, May 2015.

Other related publications by the author not included in this thesis:

Peer reviewed

1. Mikael Persson, Tomas McKelvey, Andreas Fhager, Hoi-Shun Lu, Yazdan Shirvany, Artur Chodorowski, **Qaiser Mahmood**, Fredrik Edelvik, Magnus Thordstein, Anders Hedström, Mikael Elam, "Advances in Neuro Diagnostic Based on Microwave Technology, Transcranial Magnetic Stimulation and EEG source localization", *Proceedings of Asia-Pacific Microwave Conference*, Melbourne, Australia, 5th-8th Dec., 2011.
2. Yazdan Shirvany, Fredrik Edelvik, Stefan Jakobsson, Anders Hedström, **Qaiser Mahmood**, Artur Chodorowski and Mikael Persson, "Non-invasive EEG source localization with Particle Swarm Optimization: Clinical Test", *Proceedings International Conference of the IEEE Engineering in Medicine and Biology Society (EMBC)*, pp. 6232-6235, San Diego, 22nd Aug.-1st Sep., 2012.
3. **Qaiser Mahmood**, Yazdan Shirvany, Andrew Mehnert, Artur Chodorowski, Johanna Gellermann, Fredrik Edelvik, Anders Hedström, Mikael Persson, "On the Fully Automatic Construction of a Realistic Head Model for EEG Source Localization", *Proceedings of International Conference of the IEEE Engineering in Medicine and Biology Society (EMBC)*, pp. 3331-3334, Osaka, Japan, 3rd-7th, July 2013.
4. **Qaiser Mahmood**, Artur Chodorowski, Babak Ehteshami Bejnordi, Mikael Persson, "A Fully Automatic Unsupervised Segmentation Framework for the Brain Tissues in MR Images", *SPIE Medical Imaging, Biomedical Applications in Molecular, Structural, and Functional Imaging*, Volume 9038, 2014.

Non peer reviewed

1. **Qaiser Mahmood**, Artur Chodorowski, Mikael Persson, "Adaptive Segmentation of Brain Tissues from MR Images", *Proceedings of Medicinteknikdagarna*, p.86, Linköping, Sweden, 11th-12th Oct., 2011.
2. **Qaiser Mahmood**, Artur Chodorowski, Andrew Mehnert, Johanna Gellermann, Mikael Persson, "Bayesian Based Adaptive Mean Shift Algorithm for Automatic Multi-Tissue Segmentation of the Human Head", *Proceedings of Medicinteknikdagarna*, p.158, Lund, Sweden, 2nd-3rd Oct., 2012.
3. **Qaiser Mahmood**, Yazdan Shirvany, Andrew Mehnert, Artur Chodorowski, Johanna Gellermann, Fredrik Edelvik, Anders Hedström, Mikael Persson, "On the Fully Automatic Construction of a Realistic Head Model for EEG Source Localization", *Proceedings of Swedish Symposium on Image Analysis (SSBA)*, Göteborg, Sweden, 14th-15th March, 2013.
4. **Qaiser Mahmood**, Artur Chodorowski, Mikael Persson, "Multi-modal Tumor Brain Segmentation", *Röntgennvecka*, Uppsala, Sweden, 2nd-6th Sept, 2013.
5. **Qaiser Mahmood**, Artur Chodorowski, Mikael Persson, "A Fully Automatic Unsupervised Segmentation Framework for the Brain Tissues in MR Images", *Proceedings of Medicinteknikdagarna*, Göteborg, Sweden, 14th-16th Oct., 2014.

Acknowledgments

I would like to express my gratitude to all those who gave me the possibility to complete this thesis.

First of all I would like to thank my supervisor Prof. Mikael Persson for his support throughout the research work and giving the freedom to pursue the research directions I am interested in. I would like to express my deep gratitude to Dr. Artur Chodorowski and Associate Prof. Andrew Mehnert, my co-supervisors, for their patient guidance, enthusiastic encouragement and useful critiques of this research work. I would like to express my very great appreciation to Dr. Johanna Gellermann for generating real patient ground truth images and also for sharing with me her wide MRI expertise in numerous interesting discussions. I would like also to thank Associate Prof. Fredrik Edelvik from Fraunhofer-Chalmers Research Center and Dr. Yazdan Shirvany for giving me the opportunity to apply this work to the EEG source localization problem in epilepsy. I am very grateful to Associate Prof. Andreas Fhager from Department of Signals and Systems at Chalmers University of Technology for his valuable feedback and enthusiasm with pushing this work towards stroke detection. I would like to acknowledge the Department of Clinical Neurophysiology at Sahlgrenska University Hospital, Gothenburg for providing real MRI patient data. I extend a special thanks to Dr. Irene Perini for her advice and input on the anatomy of the human head.

I would like to thank to Dr. Markus Johansson, Dr. Stefan Candefjord, Prof. Rolf Heckemann, Associate Prof. Justin Schneiderman and Henrik Mindedal from MedTech West at Sahlgrenska University Hospital and all colleagues, in particular Ann-Christine Lindbom and Natasha Adler from Department of Signals and Systems at Chalmers University of Technology for their kindness, cooperation, and support. I wish to thank all my friends especially Shahid Nawaz, Qaisar, Mohammad Alipoor, Mats Lindström, Georgi, Martina, Rhys Lewis, Cristina, Ramin and Babak for their support and creating enjoyable moments in my life. I am grateful to the Higher Education Commission (HEC) of Pakistan and Chalmers University of Technology, Sweden for providing me the scholarship to conduct this research.

Most importantly, none of this would have been possible without the love and patience of my family. I would like to express my heart felt gratitude to my loving parents, brothers and sisters and their families for their support and encouragement.

Qaiser Mahmood, Gothenburg, 2016

Abbreviations and Acronyms

AMS	Adaptive Mean Shift
BAMS	Bayesian-Based Adaptive Mean Shift
BET	Brain Extraction Tool
BT	Brain Tissue
CSF	Cerebrospinal Fluid
CT	Computed Tomography
DI	Dice Index
EEG	Electroencephalography
EM	Expectation Maximization
FAST	FMRIB's Automated Segmentation Tool
FCM	Fuzzy *C*-Means
FID	Free Induction Decay
FDTD	Finite Difference Time Domain
FMRIB	Functional MRI of the Brain
FSL	FMRIB Software Library
GE	Gradient Echo
GM	Gray Matter
GMM	Gaussian Mixture Model
GT	Ground Truth
HMRF	Hidden Markov Random Field
HSA	Hierarchical Segmentation Approach
IBSR	Internet Brain Segmentation Repository
ICM	Iterated Conditional Modes
LE	Localization Error
MRF	Markov Random Field
MRI	Magnetic Resonance Imaging
MTSA	Multi-tissue Segmentation Algorithm
MS	Mean Shift
NBT	Non-Brain Tissue
OE	Orientation Error
PD	Proton Density
PVC	Partial Volume Classifier
RE	Relative Error
RF	Radio Frequency
SPM	Statistical Parametric Mapping

SE	Spin Echo
T1	Longitudinal Relaxation Time
T2	Transverse Relaxation Time
TE	Echo Time
TR	Repetition Time
WM	White Matter
WHSA	Whole Head Segmentation Algorithm

Contents

Part I
Introductory Chapters

CHAPTER 1

Introduction

1.1 Background and problem definition

Medical imaging [1–3] is the visualization of body parts, tissues, or organs, for use in clinical diagnosis, treatment and disease monitoring. It plays an important role in the global healthcare system as it contributes to improved patient outcomes and more cost-efficient healthcare across all major diseases.

Neuroimaging [4, 5] is an important branch of medical imaging. It encompasses a range of techniques used to non-invasively image the brain at all levels of structure and function, ranging from neurotransmitter and receptor molecules to large networks of brain cells. Neuroimaging can be broadly classified into functional imaging and structural imaging.

Functional imaging [6] is used to visualize/assess the neural activity in the brain. The neural activity at a specific location in the brain is associated with localized vascular changes (such as cerebral blood flow) and metabolic changes (such as glucose and oxygen consumption). Functional imaging techniques include positron emission tomography (PET) [7], functional magnetic resonance imaging (fMRI) [8], magnetoencephalography (MEG) [9], and electroencephalography (EEG) [10].

Structural imaging [11] is used to visualize/assess anatomical structures in the brain and the head and to diagnose/characterize tumors and injuries. Structural imaging techniques include X-ray computed tomography (CT) [12] and magnetic resonance imaging (MRI) [13].

MRI has an important advantage over CT in that it does not use ionizing radiation. It generates a 3D image of the human head by exploiting the nuclear magnetic resonance properties of the water (hydrogen) contained in the tissues. Because of its high spatial resolution and good contrast for soft tissues, MRI is perfectly suited in many applications in neuroscience. Examples include the study of brain development in normal and high risk children [14, 15], the mapping of functional activation onto brain anatomy [16], and the analysis of neuroanatomical variability among normal brains [17]. For these studies, quantitative characterization of anatomical structures in the MR images is required. To achieve this, segmentation (i.e. delineation or labeling) of the brain into three major tissue types —white matter, gray matter and cerebrospinal fluid —in MR images is crucial.

Segmentation of MR brain images is also helpful for neurosurgeons and physicians in assessing the progress or remission of various neurological diseases such as Alzheimers disease, epilepsy, multiple sclerosis, and schizophrenia [18] as well as in pre-surgical evaluation and planning [16, 17].

Segmentation in MR head images also makes it possible to assign dielectric or biomechanical properties to the individual tissues to construct a dielectric or biomechanical head model, crucial for electromagnetic or biomechanical simulations. Electromagnetic modeling finds use in applications such as non-invasive EEG source localization in epilepsy patients [19], microwave imaging for stroke detection [20], hyperthermia treatment planning for head and neck tumors [21], the study of electric fields induced by transcranial magnetic stimulation (TMS) [22] and the study of deep brain simulation [23]. Biomechanical modeling finds use in applications such as brain deformation simulation for image-guided neurosurgery [24] and the study of head trauma in traffic accidents [25].

Accurate segmentation of tissues in MRI images is a challenging task because of several factors including: (i) the complexity and variability of the underlying anatomy; (ii) noise; (iii) the bias field (an unwanted low-frequency signal occurring due to inhomogeneities in the magnetic fields of the MRI scanner); (iv) scanner specificity of MRI; and (v) the low contrast between the skull, cerebrospinal fluid and air in T1-weighted MRI data. As a result many areas of the clinical research [19, 20, 22, 26–37] still largely rely on expert manual correction or intervention for anatomical structure segmentation. However, this is time consuming, subjective, tedious, and labor intensive as well as requires expert supervision and impractical for large-scale group study. Thus a fully automatic and accurate segmentation method is highly desirable.

1.2 Aim and objectives

The aim of this thesis was to develop fully automatic and accurate patient-specific tissue segmentation methods for the brain as well as for the whole-head for two important neuroimaging applications: Non-invasive EEG source localization and intracerebral hemorrhage detection in stroke patients using single and multi-modal MR images (MR images of the same anatomy but acquired using different contrast mechanisms such as T1-weighting, T2-weighting, and proton density weighting).
To this end the thesis had the following objectives:

1. To develop an unsupervised framework for segmenting the brain into individual tissue types: white matter, gray matter and cerebrospinal fluid.

2. To evaluate the performance of the proposed framework using both synthetic and real MR images of the brain.

3. To develop an unsupervised framework for segmenting the whole-head into individual tissue types: white matter, gray matter, cerebrospinal fluid, fat, muscle, skin and skull, or white matter, gray matter, cerebrospinal fluid, skin and skull.

4. To evaluate the performance of the proposed framework using both synthetic and real MR images of the head.

5. To evaluate the performance of the unsupervised whole-head segmentation framework in the context of non-invasive EEG source localization.

6. To evaluate the performance of the unsupervised whole-head segmentation framework in the context of intracerebral hemorrhage detection in stroke patients using a microwave-imaging system.

1.3 Scope of the thesis

Only unsupervised image segmentation techniques were considered in this thesis. Such techniques [38] do not require training data but rather explore the intrinsic structure of the image data using various statistics.

Supervised segmentation techniques [38,39] and multi-atlas based segmentation methods [40] were not investigated. The former requires labeled training data to extract the features and train a classifier. The classifier is then used to label unseen pixels. The latter requires many labeled images in order to define an atlas. For such methods, selection of the atlas or atlases, is crucial for improving segmentation results, for a given pathology, for instance [40, 41].

The real and synthetic MRI data sets used in this study comprised at most three different MRI modalities. The use of additional imaging modalities, such as X-ray computed tomography or ultrasound [42], was not investigated.

1.4 Overview of the thesis

The thesis is organized into two main parts.
Part I consists of chapters 2 through 8. Chapter 2 provides the basic anatomical and methodological concepts needed for the remainder of the thesis. Chapter 3 describes the reviewed literature for brain segmentation and addresses objectives 1 and 2. Chapter 4 describes the motivation for automated whole-head segmentation and addresses objectives 3 and 4. Chapter 5 evaluates the automated whole-head segmentation for EEG source localization and addresses objective 5. Chapter 6 evaluates the automated whole-head segmentation for stroke detection and addresses objective 6. A brief summary of the appended papers is presented in chapter 7, while concluding remarks and discussions of future work are presented in Chapter 8.
Part II comprises the published papers, arising from this research.

CHAPTER 2

Theoretical Background

The purpose of this chapter is to acquaint the reader with the basic anatomical and theoretical concepts essential for an understanding of the material presented in subsequent chapters. In particular, the next section presents an overview of the anatomy of the human head, section 2.2 provides an overview of magnetic resonance imaging, and finally section 2.3 describes several segmentation techniques underlying existing approaches to brain and whole-head segmentation.

2.1 Anatomy of the human head

This section provides an overview of the anatomy of the human head. The level of detail provided is sufficient for the aim and objectives of this thesis. For a more detailed and comprehensive treatment of the subject, the reader is referred to [43–45].

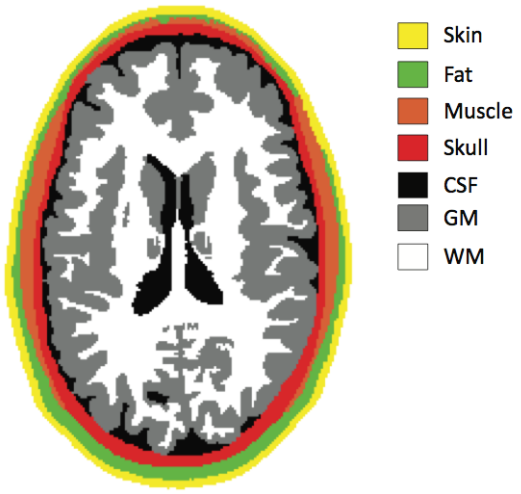

Figure 2.1: Axial slice through the human head showing the major tissue types: white matter (WM) in white, gray matter (GM) in gray, cerebrospinal fluid (CSF) in black, skull in red, fat in green, muscle in brown and skin in yellow.

The human head is made up of numerous complex tissue types and structures [28]. However it can be decomposed into the following major tissue types: white matter (WM), gray matter (GM), cerebrospinal fluid (CSF), skin, fat, muscle, and skull (as shown in Fig. 2.1). These in turn can be classified as belonging to two major classes: brain and non-brain.

2.1.1 Brain

The human brain is an important part of the central nervous system. Functionally, it can be decomposed into three main parts (see Fig. 2.2):

1. Cerebrum: This is the largest part of the brain and is composed of left and right hemispheres. Each hemisphere can in turn be divided into four lobes:
   - Frontal Lobe: It is involved in functions such as reasoning, planning, parts of speech, voluntary motor function of skeletal muscles, emotions, and problem solving.
   - Parietal Lobe: It is involved in functions such as movement, orientation, recognition, and perception of stimuli.
   - Occipital Lobe: It is involved in visual processing.
   - Temporal Lobe: It is involved in functions such as perception and recognition of auditory stimuli, memory, speech, and smell.
2. Cerebellum: It is located under the cerebrum and is involved in functions such as regulation and coordination of movement, posture, and balance.
3. Brain Stem: It is responsible for regulating breathing, heartbeat, and blood pressure.

Structurally, the brain can be decomposed into three main tissue types (shown in Fig. 2.1):

Gray matter

The gray matter is located on the thin outer layer of the brain, called the cerebral cortex, and also deeper in the brain underneath the white matter. It comprises neuronal cell bodies. Gray matter is involved in various functions including muscle control, speech, emotion, memory, vision and hearing.

White matter

The white matter lies underneath the cerebral cortex and is made up of glial cells and bundles of myelinated axons. The white matter connects various regions of the gray matter, favoring communication between cortical-cortical or cortical-subcortical structures.

Cerebrospinal fluid (CSF)

The CSF is a colorless fluid. It is located in the subarachnoid space (space between the two protective membranes that surround the brain: arachnoid membrane and pia mater), the ventricles (large cavities inside the brain) and the spinal cord. It serves to protect the brain, supply it with nutrition, and to remove waste.

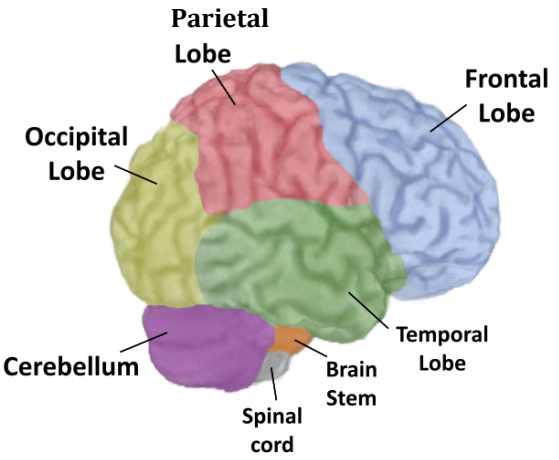

Figure 2.2: Anatomy of the human brain.

2.1.2 Non-brain

The non-brain is composed of four main tissues:

Skull

The skull is a bony structure and has a thickness between 4 to 7 mm. It surrounds the brain, eyes, nose and teeth and serves to protect them.

Skin

The scalp, neck and face surrounding the skull are composed of a soft tissue called skin. The skin is made up of two primary layers: epidermis and dermis. The epidermis layer is the outermost layer of the skin and acts as infection barrier. The dermis layer lies underneath the epidermis and provides tensile strength and elasticity to the skin.

Fat

Fat is a soft tissue that lies beneath the skin. It is made up of adipose cells called adipocytes.

Muscle

The term muscle describes another soft tissue located inside the skin. It is composed of protein filaments that slide past one another enabling actions such as eating, blinking and smiling.

2.2 Magnetic Resonance Imaging (MRI)

This section provides a brief overview of the principles of magnetic resonance imaging (MRI). For a more detailed and comprehensive treatment see [46–49].

MRI is a non-invasive imaging technique. R. Damadian, in 1971, proposed MRI for use as a medical imaging device. In 2003, P. Lauterbur and P. Mansfield received the Noble prize in Physiology or Medicine for their pioneering work in the development of

MRI.

MRI is based on a physical phenomenon called nuclear magnetic resonance, which is defined as the ability of magnetic nuclei to absorb energy from an electromagnetic pulse and to radiate this energy back. The hydrogen nucleus or proton is positively charged and possesses an angular moment called spin. This property causes it to behave as a tiny magnet with a small magnetic field or magnetic moment.

In MR imaging the object to be imaged is placed inside a strong external magnetic field $\mathbf{B}_0$ that causes the protons either to align with $\mathbf{B}_0$ or opposed to it. The small difference in the two populations yields a bulk magnetization $\mathbf{M}$, which is the sum of the individual magnetic moments of the individual protons, that depends linearly on the field intensity and is aligned with the $\mathbf{B}_0$ field (illustrated in Fig. 2.3). This state of magnetization is known as thermal equilibrium.

The magnetization vector $\mathbf{M}$ is the main source of the MR signal and is used to produce an MR image. It has two components called longitudinal and transverse magnetization. The longitudinal magnetization (denoted as $\mathbf{M}_z$) is parallel to the external magnetic field $\mathbf{B}_0$ while the transverse magnetization (denoted as $\mathbf{M}_{xy}$) is perpendicular to the $\mathbf{B}_0$.

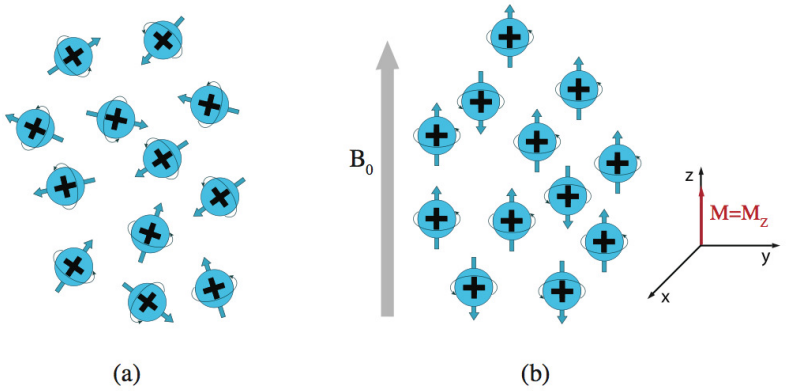

Figure 2.3: Alignment of protons with the $\mathbf{B}_0$ field: (a) with no external magnetic field, all the protons are oriented randomly (b) in the presence of external magnetic field ($\mathbf{B}_0$), some of the protons align with the field (parallel to the external magnetic field $\mathbf{B}_0$) whilst some of these oppose to the field (anti-parallel to $\mathbf{B}_0$). As a result, a net magnetization $\mathbf{M} = \mathbf{M}_z$ is produced parallel to the external field $\mathbf{B}_0$. As a result, a net magnetization $\mathbf{M} = \mathbf{M}_z$ is produced parallel to the external field $\mathbf{B}_0$ (adapted from [49]).

When a radio frequency (RF) pulse $\mathbf{B}_{\mathrm{RF}}$ (having frequency equal to the Larmor frequency) is applied, it gives energy to the protons. As a result, the magnetization vector $\mathbf{M}$ flips in the transverse plane and the longitudinal component $\mathbf{M}_z$ becomes zero. Once the RF pulse is turned off, another RF signal is generated by the protons due to the magnetic resonance phenomena. This signal is decaying towards zero when the magnetization vector $\mathbf{M} = \mathbf{M}_{xy}$ in the transverse plane starts to dephase. This state is known as transverse relaxation or T2-relaxation. The dephasing of $\mathbf{M}_{xy}$ is due to the magnetic moments of pro-

tons that are precessing with slightly different frequencies. The decaying signal is known as free induction decay (FID) which is measured by a conductive field coil in the MR scanner and then it is processed to get the MR image of the object. After T2-relaxation, the protons build up the magnetization vector $\mathbf{M} = \mathbf{M}_z$ again parallel to the original $\mathbf{B}_0$ field and the state is known as longitudinal relaxation or T1-relaxation. The illustration of T2- and T1-relaxation are shown in Fig. 2.4 and Fig. 2.5 respectively.

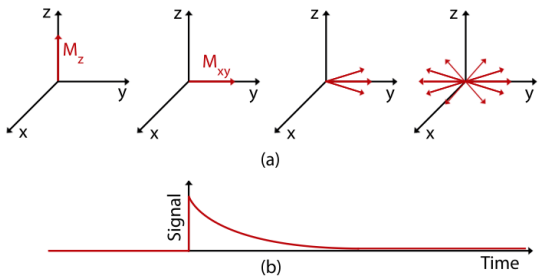

Figure 2.4: T2- relaxation: (a) Flipping of $\mathbf{M}_z$ from longitudinal plane and dephasing of $\mathbf{M}_{xy}$ in the transverse plane (b) Free induction decay (FID).

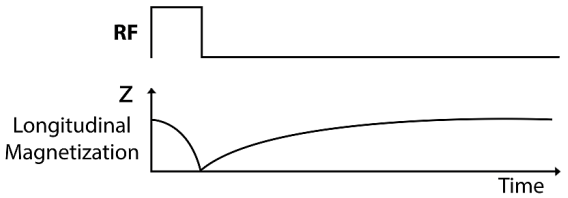

Figure 2.5: T1- relaxation: Application of 90° RF pulse causes longitudinal magnetization $\mathbf{M}_z$ to become zero. Over time, the longitudinal magnetization $\mathbf{M}_z$ will grow back in a direction parallel to the main $\mathbf{B}_0$ field.

Mathematically, the decaying of transverse magnetization $\mathbf{M}_{xy}$ during the T2-relaxation and the growing of longitudinal magnetization $\mathbf{M}_z$ during the T1-relaxation can be expressed as

$$\mathbf{M}_{xy}(t) = \mathbf{M}_{xy0} e^{-t/T2} \tag{2.1}$$

$$\mathbf{M}_z(t) = \mathbf{M}_0 (1 - e^{-t/T1}) \tag{2.2}$$

where $\mathbf{M}_{xy0}$ is the transverse magnetization at time t=0 and $\mathbf{M}_0$ is the longitudinal magnetization at time t=0.
The above equations are solutions of the Bloch equations, introduced by Felix Bloch [50].

2D and 3D MR imaging

In MRI, two approaches called 2D and 3D imaging can be used to acquire a 3D image of an object. In 2D imaging, the RF pulse is used to excite only the selected slice of an object. In this way the signal generated from that particular slice is used to construct the image of that slice. In 3D imaging, the volume of an object that contains the stack of slices is excited with the RF pulse to get the image of that particular volume of an object.

2.2.1 Contrast Mechanisms in MRI

In MRI, the contrast between tissues is based on the intrinsic properties of the tissues; namely proton density (PD), T1 and T2.

T1 is defined as the time that it takes the longitudinal magnetization $\mathbf{M}_z$ to grow back to 63% of its original value. It is related to the rate of regrowth of longitudinal magnetization which is a fundamental source of contrast in T1-weighted images. Different tissues have different rates of T1-relaxation, shown in Fig. 2.6.

T2 is defined as the time that it takes the transverse magnetization $\mathbf{M}_{xy}$ to decrease to 37% of its starting value. It is related to the rate of dephasing of transverse magnetization that is a fundamental source of contrast in T2-weighted images. Different tissues have different rates of T2-relaxation, shown in Fig. 2.7.

PD refers to the density of protons in the tissues. Different tissues have different density of protons.

The weighting amount of T1 and T2 effects in the MR images, is controlled by two basic scanning parameters known as echo time (TE) and repetition time (TR). TE is defined as the time between the start of the RF pulse and the maximum in the FID response signal. TR is defined as the time between the consecutive RF pulses.

The relative values of TE and TR to produce different contrast weighted images are shown in Fig. 2.8. A T1-weighted image is produced by maximizing the T1-relaxation and minimizing the T2-relaxation using short TE and intermediate TR. A T2-weighted image is produced by maximizing the T2-relaxation and minimizing the T1-relaxation using long TE and long TR. A PD-weighted image is produced by minimizing the both T1- and T2-relaxation using short TE and long TR.

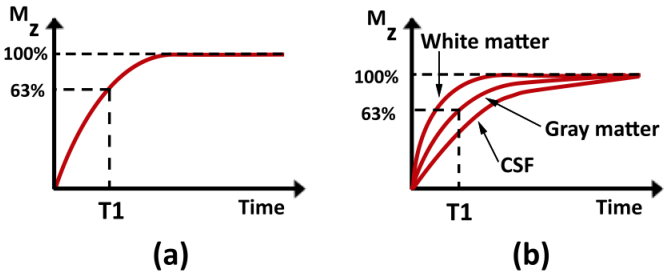

Figure 2.6: (a) T1: longitudinal magnetization increases to 63% of maximal $\mathbf{M}_z$ (b) Different tissues have different rates of T1-relaxation.

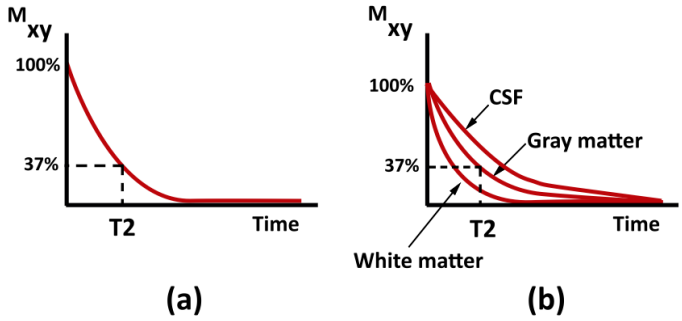

Figure 2.7: (a) T2: transverse magnetization decreases to 37% of the starting value of $\mathbf{M}_{xy}$ (b) Different tissues have different rates of T2-relaxation.

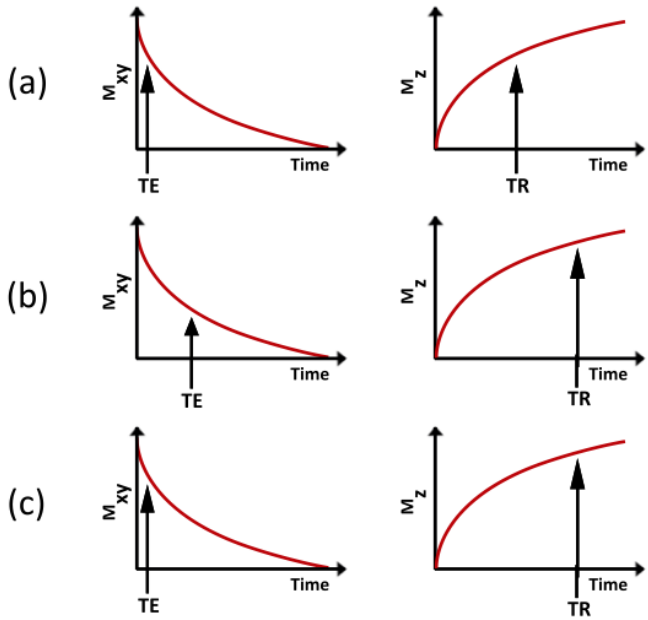

Figure 2.8: Scanning parameters: (a) short TE and intermediatory TR for T1-weighting (b) long TE and long TR for T2-weighting (c) short TE and long TR for PD-weighting.

Tissues of the human head visualized by magnetic resonance imaging

Fig. 2.9 shows three MR images of same axial slice through a human head. In these images the contrast between soft tissues can be seen clearly. The contrast in these images are characterised as (a) T1-weighted (b) T2-weighted (c) PD-weighted. In the T1-weighted image the CSF, skull, and fat appear dark and the gray matter, white matter, skin and

muscle appear bright. In the T2-weighted image the CSF and skin appear bright, and the skull, fat, muscle, white matter and gray matter appear darker than in the T1-weighted image. In the PD-weighted image the fat, muscle, white matter, gray matter, and CSF appear bright, and the skull appears dark.

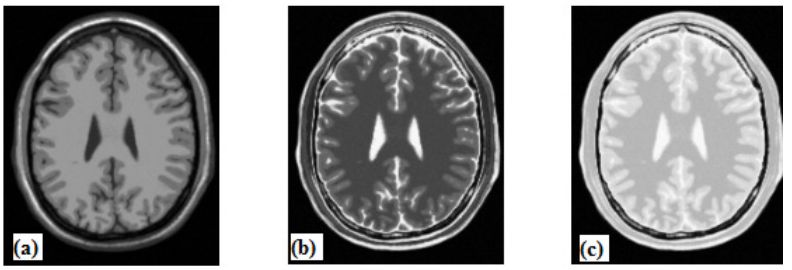

Figure 2.9: Axial slice from an MRI scan of the human head ([51]) (a) T1-weighted (b) T2-weighted (c) PD-weighted image.

2.2.2 Basic pulse sequences for MRI

Two pulse sequences known as spin echo (SE) and gradient echo (GE) are commonly used to generate MR images. These sequences are repeated many times during a scan to generate the image of an object.

In a spin echo sequence, a 90° RF pulse is used to flip the magnetization vector $\mathbf{M}$ in the transverse plane. As the protons go through the T1- and T2- relaxation, the transverse magnetization $\mathbf{M}_{xy}$ is gradually dephased. A 180° RF pulse is applied to rephase it. As a result, a signal (called spin echo) is generated and is used to reconstruct an MR image. In order to generate the different contrast MR images, SE sequence is based on the TE and TR scanning parameters.

In gradient echo sequence, an RF pulse is applied that partly flips the net magnetization vector $\mathbf{M}$ into the transverse plane. A negative gradient pulse is used to dephase the transverse magnetization $\mathbf{M}_{xy}$ and a positive gradient pulse is applied to rephase it. As a result, a signal (called gradient echo) is generated. In a GE sequence, the scanning parameters: flip angle, TE, and TR are used to produce different contrast MR images. However, in this thesis the MR images were acquired by applying the gradient echo pulse sequence.

2.2.3 Artifacts in MRI

The two major sources of artifacts that degrade MR image quality significantly and also obfuscate the anatomical and physiological detail are noise and the bias field. The noise in MRI is generally caused by the thermal agitation of electrons in the conductor. It is usually modeled as Rician distribution [52]. The bias field is a low frequency smooth undesirable signal which is caused by inhomogeneities in the magnetic field of the MR scanner. It changes the intensity values of the image pixels so that the same tissue has different gray level distribution across the image.

2.3 Overview of the basic segmentation techniques underlying existing approaches to brain and whole-head segmentation

Image segmentation refers to the process where every pixel in a digital image is assigned a label and such that pixels sharing the same characteristics are given the same label. Numerous techniques for image segmentation can be found in the literature [53]. No single technique is applicable for all problems and no general theory exists for synthesizing a segmentation solution for any given problem. The image analysis practitioner must therefore devise solutions based on one or more techniques and using experience and trial and error.
In this section we give a brief description of the elementary segmentation techniques used in the brain and whole-head segmentation methods presented/discussed in later chapters.

Mean Shift

Mean shift is a non-parametric mode seeking and clustering technique originally proposed by Fukunaga and Hostetler [54]. Its application to image processing and computer vision tasks such as filtering, image segmentation and real time object tracking was pioneered by Comaniciu et al. [55].

Mean shift does not require any prior information concerning the number of clusters, and does not constrain the size or shape of the clusters. Mean shift clustering is based on an adaptive gradient ascent approach to estimate the local maxima or modes of multivariate distributions underlying the feature space. Ultimately each feature point is associated with a mode thereby defining clusters. The basic principle of mean shift clustering is described below.

Let $\{\mathbf{x}_i \in \mathbb{R}^d | i = 1.....n\}$ denote a set of feature vectors (data points) in d- dimensional space. The kernel density estimate of the underlying multivariate probability function at point $\mathbf{x}$ is given by

$$\hat{f}_K(\mathbf{x}) = \frac{1}{n}\sum_{i=1}^{n} |\mathbf{H}|^{-1/2} K(|\mathbf{H}|^{-1/2}(\mathbf{x}-\mathbf{x}_i)) \tag{2.3}$$

where $\mathbf{H}$ is a $d \times d$ symmetric positive definite bandwidth matrix. For a radially symmetric kernel, $\mathbf{H} = h^2\mathbf{I}$ which leads to

$$\hat{f}_K(\mathbf{x}) = \frac{c_{k,d}}{nh^d}\sum_{i=1}^{n} k\left(\left\|\frac{\mathbf{x}-\mathbf{x}_i}{h}\right\|^2\right) \tag{2.4}$$

where $h > 0$ is a scalar bandwidth and $k : [0,1] \to \mathbb{R}$ is the kernel profile of the radially symmetric kernel K with bounded support defined as

$$K(\mathbf{x}) = c_{k,d}\, k\left(\|\mathbf{x}\|^2\right) \qquad \|\mathbf{x}\| \leq 1 \tag{2.5}$$

and $c_{k,d}$ is a normalizing constant ensuring that the kernel K integrates to 1. The typical kernels used in the mean shift applications are Gaussian K_G and Epanechnikov K_E given

as

$$K_G(\mathbf{x}) = c_{k,d} k_G = c_{k,d} \exp\left(-\frac{1}{2}\|\mathbf{x}\|^2\right) \tag{2.6}$$

$$K_E(\mathbf{x}) = c_{k,d} k_E = c_{k,d}(1 - \|\mathbf{x}\|^2) \qquad \|\mathbf{x}\| \leq 1 \tag{2.7}$$

where k_G and k_E are the kernel profiles of K_G and K_E respectively. The derivative of the sample point density estimator in eq. 2.2 leads to

$$\hat{\nabla} f_K(\mathbf{x}) \equiv \nabla \hat{f}_K(\mathbf{x}) = \frac{2c_{k,d}}{nh^{d+2}} \sum_{i=1}^{n} (\mathbf{x} - \mathbf{x}_i) k'\left(\left\|\frac{\mathbf{x} - \mathbf{x}_i}{h}\right\|^2\right) \tag{2.8}$$

$$= \frac{2c_{k,d}}{nh^{d+2}} \left[\sum_{i=1}^{n} g\left(\left\|\frac{\mathbf{x} - \mathbf{x}_i}{h}\right\|^2\right)\right] \times \left[\frac{\sum_{i=1}^{n} \mathbf{x}_i g\left(\left\|\frac{\mathbf{x}-\mathbf{x}_i}{h}\right\|^2\right)}{\sum_{i=1}^{n} g\left(\left\|\frac{\mathbf{x}-\mathbf{x}_i}{h}\right\|^2\right)} - \mathbf{x}\right] \tag{2.9}$$

where $g(x) = -k'(x)$ is the derivative of kernel profile k. The second factor in eq. 2.9 is called the mean shift vector. It points toward the direction of maximum increase in density and also provides the basis for clustering. The mean shift vector can be written as

$$M_{h,G}(\mathbf{x}) = \frac{\nabla \hat{f}_K(\mathbf{x})}{\hat{f}_G(\mathbf{x})} = \frac{\sum_{i=1}^{n} \mathbf{x}_i g\left(\left\|\frac{\mathbf{x}-\mathbf{x}_i}{h}\right\|^2\right)}{\sum_{i=1}^{n} g\left(\left\|\frac{\mathbf{x}-\mathbf{x}_i}{h}\right\|^2\right)} - \mathbf{x} \tag{2.10}$$

where G represents the kernel and is defined as

$$G(\mathbf{x}) = c_{g,d} g(\|\mathbf{x}\|^2) \tag{2.11}$$

The kernel G starts from an initial position $\mathbf{y}_1$ and moves towards the position closer to the higher density region. The update rule of kernel position is given by

$$\mathbf{y}_{j+1} = \frac{\sum_{i=1}^{n} \mathbf{x}_i g\left(\left\|\frac{\mathbf{y}_j - \mathbf{x}_i}{h}\right\|^2\right)}{\sum_{i=1}^{n} g\left(\left\|\frac{\mathbf{y}_j - \mathbf{x}_i}{h}\right\|^2\right)}, \quad j = 1, 2, ... \tag{2.12}$$

where $\{\mathbf{y}_j\}_{j=1,2,...}$ represents the successive locations of the kernel G. The guaranteed convergence of the mean shift algorithm to the local maximum of a probability density function is obtained by the adaptive magnitude of the mean shift vector $M_{h,G}(\mathbf{x})$. In a lower density region, the magnitude of $M_{h,G}(\mathbf{x})$ is large, and in a high density region (i.e. closer to a mode), the magnitude is small. The speed of convergence depends on the kernel type. The feature (data) points that converge to the same mode constitute a cluster.

To apply the mean shift clustering to the problem of image segmentation, one represents each pixel as a feature point $\mathbf{x}_i$ formed by concatenating its spatial coordinates and range (intensity) values (e.g., T1 and T2-weighted) and employs the following joint

spatial-range domain kernel $K_{h_s,h_r}(\mathbf{x})$ defined

$$K_{h_s,h_r}(\mathbf{x}) = \frac{C}{h_s^p h_r^d} k\left(\left\|\frac{\mathbf{x}^s}{h_s}\right\|^2\right) k\left(\left\|\frac{\mathbf{x}^r}{h_r}\right\|^2\right) \tag{2.13}$$

where $\mathbf{x}^s$ represents a vector of pixels spatial coordinates, $\mathbf{x}^r$ represents a vector of pixels range (intensity) values and h_s and h_r are their corresponding kernel bandwidths and C is the normalization constant.

An example of mean shift (MS) clustering for 2D intensity feature space is illustrated in Fig. 2.10.

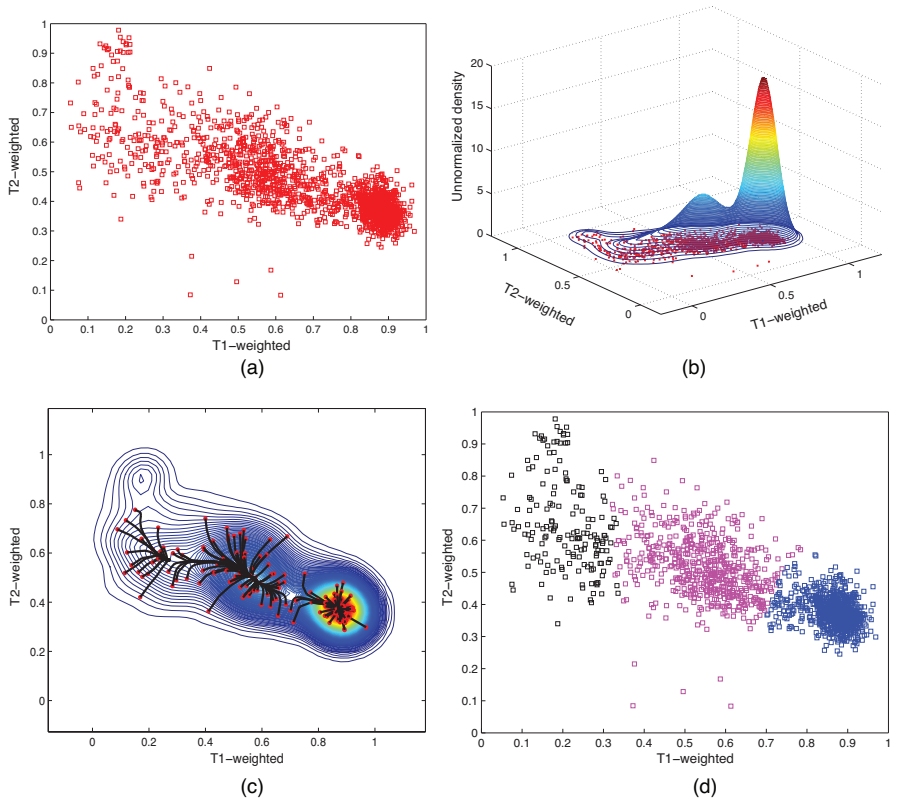

Figure 2.10: (a) The 2D feature space for data from a multi-modal MR image (T1- and T2-weighted) (b) Estimated density distribution using a Gaussian kernel with bandwidth $h = 0.08$ (c) Mean shift procedure trajectories for some feature points. (d) Resulting clusters after applying mean shift (CSF in black, gray matter in magenta and white matter in blue).

k-means Algorithm

The standard k-means algorithm was introduced by MacQueen [56,57] in 1967 to describe one of the simplest unsupervised clustering algorithms. In this algorithm, the partitioning of n data points into k disjoint subsets S_j is done by minimizing the following cost function

$$J = \sum_{j=1}^{k} \sum_{i \in S_j} \|\mathbf{x}_i - \mu_j\|^2 \tag{2.14}$$

where $\mathbf{x}_i$ is a vector representing the ith data point and μ_j is the centroid of the data points in S_j.

The standard k-means algorithm starts with random initialization of k centroids. Each data point is then assigned to the closest centroid and the number of data points closest to a centroid form a cluster. The new centroid is computed according to the data points in the cluster. This process is continued until the data points stop changing their centroids or clusters. The downside of this algorithm is that it is quite sensitive to the initialization of the centroids of the clusters and it provides clustering in the intensity (range) domain only.

Fuzzy c-means

Fuzzy c-means (FCM) was introduced by Dunn [58] and later improved by Bezdek [59]. It aims to categorize each pixel in the image using fuzzy memberships.

Let $\{\boldsymbol{x}_i \in \mathbb{R}^d | i = 1.....N\}$ represent an image with N pixels to be divided into c clusters. The FCM algorithm is an iterative optimization that minimizes the cost function given by

$$J = \sum_{i=1}^{N} \sum_{j=1}^{c} p_{ij}^m \|\mathbf{x}_i - \mu_j\|^2. \tag{2.15}$$

where p_{ij} denotes the membership of pixel $\mathbf{x}_i$ in the jth cluster, μ_j is the jth cluster center, $\|.\|$ is a norm metric, and m is a constant that controls the fuzziness of the resulting partition.

The cost function is minimized when pixels close to the centroid of their clusters are assigned high membership values, and low membership values are assigned to pixels far from the centroid. The membership function represents the probability that a pixel belongs to a specific cluster. The membership functions and cluster centers are updated as follows

$$p_{ij} = \frac{1}{\sum_{k=1}^{c} \left(\frac{\|\mathbf{x}_i - \mu_j\|}{\|\mathbf{x}_i - \mu_k\|} \right)^{\frac{2}{m-1}}} \tag{2.16}$$

and

$$\mu_j = \frac{\sum_{i=1}^{N} p_{ij}^m \mathbf{x}_i}{\sum_{i=1}^{N} p_{ij}^m} \tag{2.17}$$

FCM starts with random initialization of c centroids and converges to a solution for μ_j representing the local minimum of the cost function. The convergence is detected by comparing the changes in the membership function or the cluster center at two sequential iteration steps.

Parametric Statistical Methods

Parametric statistical methods assume some distributional form for the underlying probability distribution of the image and seek to estimate its parameters. For example, the intensity of pixels in the image is typically modeled using a Gaussian mixture model (GMM) [60], which is a weighted sum of several component Gaussian densities. The GMM is parameterized by the mean vectors, covariance matrices and mixture weights from all component densities and these parameters are estimated using the Expectation-Maximization (EM) algorithm [61]. Finally, the segmentation is done by assigning every pixel to the class label for which it has the highest *a* posteriori probability.

The majority of methods that have been proposed in the literature for automated segmentation of brain tissues are based on parametric statistical models. For example, the hidden Markov random field model and associated Expectation-Maximization (HMRF-EM) algorithm is one of the state-of-the-art methods. In this algorithm, HMRF is a stochastic model generated by a Markov random field (MRF) whose state sequence is estimated indirectly through observations. The advantage of HMRF is derived from the MRF theory in which the spatial information of an image is encoded through contextual constraints of neighbouring pixels. The EM algorithm is used to fit this model. The principle of the HMRF-EM method is described below.

Let $\mathbf{y} = (y_1, ..., y_N)$ represent a gray-scale image such that y_i represents the intensity of the i-th pixel. Let $\mathbf{x} = (x_1, ..., x_N)$ represent a label image such that $x_i \in L$ is the label corresponding to pixel y_i and L is the set of all possible labels.

According to the maximum a posteriori (MAP) criterion, the optimal labeling $\hat{\mathbf{x}}$ is obtained as follows

$$\hat{\mathbf{x}} = \arg\max_{\mathbf{x}} \{P(\mathbf{y}|\mathbf{x}, \Theta)P(\mathbf{x})\} \tag{2.18}$$

where $\mathbf{x}$ is a realization of an MRF and $P(\mathbf{x})$ is its prior probability given by

$$P(\mathbf{x}) = Z^{-1} \exp(-U(\mathbf{x})) \tag{2.19}$$

where Z is a normalizing constant and $U(\mathbf{x})$ is an energy function of the form

$$U(\mathbf{x}) = \sum_{c \in C} V_c(\mathbf{x}) \tag{2.20}$$

where $V_c(\mathbf{x})$ is the clique potential and C is the set of all possible cliques. In the image, a clique c is defined as a subset of pixels in which every pair of pixels are neighbors.
$P(\mathbf{y}|\mathbf{x}, \Theta)$ represents the joint likelihood probability and is defined

$$P(\mathbf{y}|\mathbf{x},\Theta) = \prod_i P(y_i|x_i,\theta_{x_i}) \tag{2.21}$$

where $P(y_i|x_i,\theta_{x_i})$ is a Gaussian distribution with parameters $\theta_{x_i} = \{\mu_{x_i}\sigma_{x_i}\}$. $\Theta = \{\theta_l|l \in L\}$ is the set of parameters which are estimated using the EM algorithm. In [62], the iterated conditional modes (ICM) algorithm [63] (one of the optimization methods) is used to obtain the optimal solutions of MAP.

Four widely used brain tissue segmentation toolboxes: SPM (Statistical Parametric Mapping toolbox) [64, 65], PVC (Partial Volume Classifier) [66], FreeSurfer [67] and FAST (FMRIB's Automated Segmentation Tool) [62] are based on parametric statistical methods. For example, in SPM, the underlying method is based on the parameter estimations of a Gaussian mixture model (GMM), atlas registration and bias field correction at the same time iteratively. In FreeSurfer, the underlying method includes registration to a brain atlas, a Bayesian estimation theory framework, a Markov random field (MRF) spatial model and the ICM algorithm [63]. In PVC, the underlying method includes a maximum-a-posteriori (MAP) classifier and spatial prior model of the brain. In FAST, the underlying method is based on the HMRF-EM algorithm.

CHAPTER 3

MRI Brain Tissue Segmentation

This chapter addresses objectives 1 and 2 of this thesis (described in chapter 1) for segmenting the brain into three tissue types: white matter, gray matter and cerebrospinal fluid. The chapter consists of three sections. Section 3.1 presents a review of existing methods for brain tissue segmentation. The proposed unsupervised framework is presented in section 3.2. The empirical evaluation of the proposed method and the other existing unsupervised methods is presented in section 3.3.

3.1 MRI brain tissue segmentation methods: A review

Automated and accurate tissue segmentation is an important and challenging task in the quantitative analysis of brain MR images. In literature, a wide variety of automatic methods have been proposed for segmenting the brain tissues in MR images. From the perspective of machine learning, these can be broadly classified into two major types: supervised and unsupervised segmentation methods.

Supervised segmentation methods [39, 68–72] need training datasets for feature extraction and classifier training. The trained classifier is then applied to label pixels in image. However, supervised methods have a major drawback in that they require sufficiently large training dataset from a similar distribution as the data to be segmented. Consequently, in practice these methods are not suitable for data acquired with a different scanner or scanning protocol [73].

In contrast, unsupervised methods don't need any training datasets for segmentation. Various unsupervised methods have been proposed for brain tissue segmentation. Most of them are based on parametric statistical methods [18, 62, 64, 74–80], which assume some distributional form for the underlying probability distribution of the data and seek to estimate its parameters. Several of them [74–76] perform purely intensity based clustering. However, a major drawback of these is that they may give poor tissue classifications in the presence of additive noise and multiplicative bias field inherent in MR images [41]. To solve these problems, several parametric methods [18, 62, 64, 77–79] employ a Markov random field (MRF) statistical spatial model. However, the main downside of these approaches is that the MRF algorithm is computationally expensive and needs critical parameter settings in a high dimensional feature space [41].

Mean shift (MS) [54,55] is one of the unsupervised clustering methods, which doesn't have this problem. It is an adaptive gradient approach to estimate the modes of the multivariate distribution underlying the feature space. The feature points that have a common mode constitute a cluster. The kernel bandwidth is the only parameter of the MS that influences the clustering. For example, use of a small bandwidth can cause over-clustering whilst use of a large bandwidth can cause under-clustering. Numerous approaches [81,82] have been proposed to overcome this problem. These approaches employ adaptive bandwidth of the kernel to estimate the modes or clusters.

The mean shift based on the adaptive bandwidth for estimating the modes is called the adaptive mean shift (AMS) [81, 82]. AMS can perform clustering by taking both the spatial and the intensity domain into account. This characteristic can make AMS more robust to the MRI artifacts such as noise and spatial intensity inhomogeneity compared to intensity-based clustering methods [41]. AMS yields a set of clusters or modes. However, to get the desired number of clusters, merging is required. Mayer et al. [41] proposed the first adaptive mean shift framework for segmenting brain tissues in MR images. This framework used a mode pruning and voxel-weighted k-means algorithm to assign the clusters, obtained from the adaptive mean shift, into white matter (WM), gray matter (GM) and cerebrospinal fluid (CSF) tissue. However, mode pruning in the range (intensity) domain ignores the spatial information of modes/clusters, which may cause merging of the modes belonging to different tissue types. In addition, merging of pruned modes into desired tissue types using the voxel-weighted k-means algorithm, initialized by using prior knowledge of tissue intensity ordering in MR images [41], may also lead to assigning the clusters to the wrong tissue type. These collective limitations motivated the development of the new unsupervised segmentation framework presented in the next section.

3.2 Proposed unsupervised segmentation framework

We here propose a new unsupervised framework for segmenting the brain into three tissue types: WM, GM and CSF. The proposed framework is based on Bayesian adaptive mean shift, *a priori* spatial tissue probability maps and the fuzzy c-means algorithm

Bayesian adaptive mean shift is a variant of the AMS method proposed in [41]. In AMS, the adaptive bandwidth of the kernel is estimated in terms of the distance between the current feature point and its k-th nearest neighbor. However, the estimation of the kernel bandwidth using this approach can be biased by outliers [83].

In [83] a fixed (global) kernel bandwidth estimation approach is proposed to solve this problem. In the proposed framework, we employ this approach locally to estimate the adaptive bandwidth of the kernel for each feature point. The approach, called Bayesian adaptive mean-shift, uses a Bayesian method that involves fitting the Gamma distribution probability density function to the local variances of N sets of neighborhoods around the current feature point $\mathbf{x}_i$ (for more details see [83] and appendix A in paper B).

Schematic of the proposed segmentation framework

A schematic of the proposed framework is presented in Fig. 3.1. The proposed framework involves three pre-processing steps: (1) Extraction of the brain from the MRI data (T1-weighted image) using a brain binary mask, obtained from the given ground truth. (2) Bias field correction using the N3 bias field correction algorithm [84], and (3) Co-registration of *a priori* spatial tissue probability maps, obtained from the ICBM [85], to the MRI brain data (T1-weighted brain image) using Flirt registration tool in FSL [86]. The following steps are then applied to segment the brain as follows:

1. Pre-clustering using Bayesian adaptive mean shift:
   (a) The adaptive bandwidth h_i for each feature point $\mathbf{x}_i$ is estimated using the Bayesian approach as described in paper B.
   (b) The clusters of the brain tissue is then estimated, defined in Eq.2.12, using the adaptive bandwidth h_i, obtained from step 1(a). The clustering is performed in the joint spatial-intensity domain using the joint kernel defined in Eq.2.13.
2. Final clustering to the desired number of clusters using fuzzy c-means: The fuzzy c-means algorithm (as described in section 2.3) is applied to assign the clusters, obtained from step 1(b), into the WM, GM, and CSF tissue using Eq.2.15. In the fuzzy c-means algorithm, the center of the jth tissue μ_j is initialized by incorporating the *a priori* spatial tissue probability maps p_{ij} (obtained from the ICBM) using Eq.2.17.

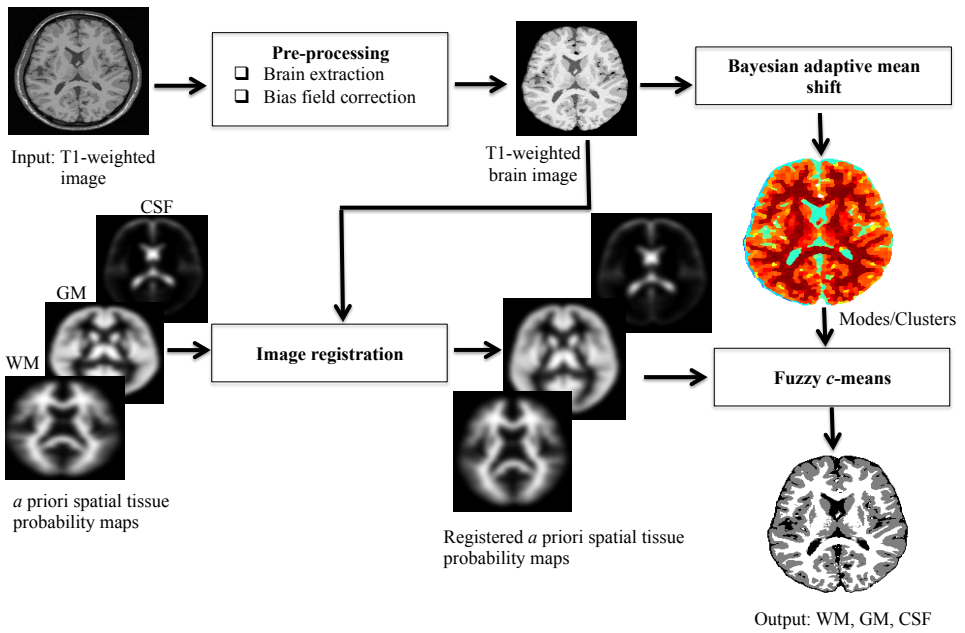

Figure 3.1: Schematic of the proposed framework.

3.3 Empirical evaluation of the proposed framework

This section summarizes the empirical evaluation, detailed in paper B, of the proposed framework. The proposed framework was validated on a synthetic T1-weighted MR image with varying noise characteristics and spatial intensity inhomogeneity, obtained from the BrainWeb database as well as on 38 real T1-weighted MR images, obtained from the IBSR repository. The performance of the proposed framework was evaluated relative to the three widely used brain segmentation toolboxes: FAST (FMRIBs Automated Segmentation Tool) [62], SPM (Statistical Parametric Mapping) [64, 65] and PVC (Partial Volume Classifier) [66], and the adaptive mean shift (AMS) [41] and classical Fuzzy c-means (FCM) [59] methods. The performance was evaluated both quantitatively and qualitatively.

Quantitative results

The quantitative performance of the proposed framework and each competing method was measured using the Dice index/score.

The Dice index/score (DI) [87] measures the degree of overlap between the ground truth and the segmentation result. It is defined as

$$DI = \frac{2V_{ae}}{V_a + V_e} \tag{3.1}$$

where V_{ae} is the number of voxels the segmentation result and the ground truth have in common, and V_a and V_e denote the number of voxels in the segmentation result and the ground truth respectively. The DI yields one for perfect overlapping and zero when there is no overlap between the segmentation result and ground truth.

The quantitative results (mean Dice index) over all the subjects for the synthetic dataset and the IBSR18 dataset are presented in paper B; see figures 4, 5 and 7 respectively. Herein, we present in detail, the quantitative results for the IBSR20 dataset with 20 subjects. The dataset was corrupted with strong intensity inhomogeneities (bias field).

The quantitative results for the IBSR20 dataset (shown in Fig. 3.2) show that across the different subjects, for the GM, the proposed method yields higher or comparable segmentation accuracy (Dice index/score) for each subject compared to all competing methods. However, for the WM, the proposed method has higher segmentation accuracy for each subject compared to all competing methods except for the subjects 2_4, 15_3, 16_3 for which SPM has higher segmentation accuracy, and the subject 2_4 for which FAST yields higher segmentation accuracy and the subject 191_3 for which FCM has higher segmentation accuracy. Moreover, for the CSF, the proposed method yields higher segmentation accuracy for each subject compared to all competing methods except for the subject 202_3 for which SPM has higher segmentation accuracy and the subject 13_3 for which AMS has higher segmentation accuracy.

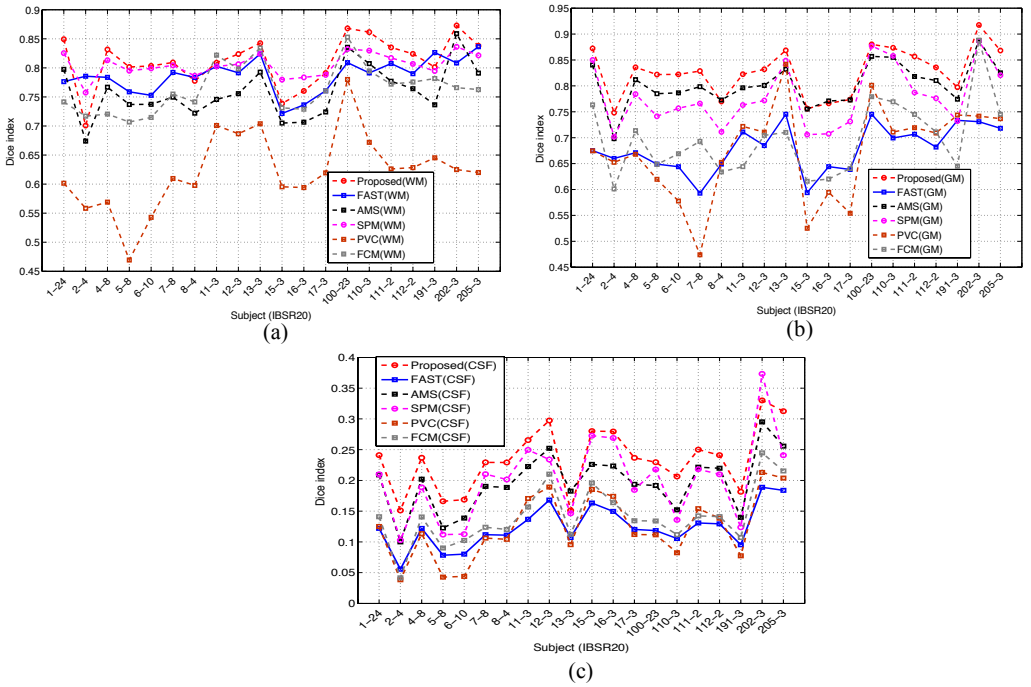

Figure 3.2: Dice index for each method for 20 subjects from the IBSR20 dataset for (a) WM (b) GM and (c) CSF.

However, over all the subjects, the quantitative results for the IBSR20 dataset (shown in Fig. 3.3) show that the proposed framework performs well (higher Dice index/score) for each tissue compared to all the competing methods. Moreover, the results for the competing methods, presented here are consistent with the results published in [88].

For the results shown in Fig. 3.2, several multiple comparison tests were done in order to determine whether there exists a statistically significant difference in the voxel-wise classification performance between the proposed framework and each of the other methods.

Each multiple comparison test involved performing five McNemar tests [89]. Each McNemar test involved computing a 2×2 contingency matrix

$$\begin{bmatrix} n_{11} & n_{12} \\ n_{21} & n_{22} \end{bmatrix} \tag{3.2}$$

where n_{11} is the number of voxels correctly classified by both methods, n_{12} is the number of voxels correctly classified by proposed framework but not the other method, n_{21} is the number of voxels incorrectly classified by proposed framework but correctly classified by the other method, and n_{22} is the number of voxels incorrectly classified by both methods.

For each McNemar test the null hypothesis was that the two methods have the same performance, i.e. $n_{11} = n_{22}$, versus the alternative hypothesis that they do not. The level of significance for each multiple comparison test was taken to be α=0.05 and so, using Bonferroni correction, the level of significance for each McNemar test was α =0.05/5

=0.01.

The McNemar tests for the IBSR20 dataset results for each tissue (shown in Fig. 3.2) provide evidence that the proposed framework is significantly different ($p\text{-}values < 0.01$) to all competing methods.

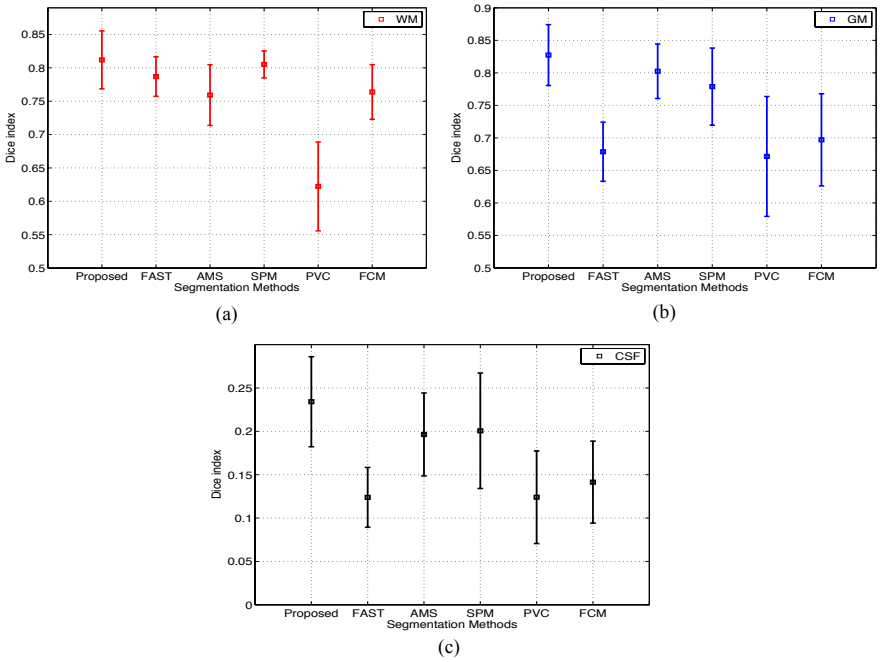

Figure 3.3: Mean Dice index for each method over the 20 subjects of the IBSR20 dataset for (a) WM (b) GM and (c) CSF. The error bars show ± 1 standard deviation.

Qualitative results

An illustration of segmentation for each method for coronal slice 31 of the subject 15_3 from the IBSR20 dataset is presented in Fig. 3.4.

It can be seen that relative to the ground truth, the proposed framework has less misclassification for the GM compared to all the competing methods. However, for the WM, the proposed framework has higher misclassification compared to SPM, especially in a region close to the ventricles.

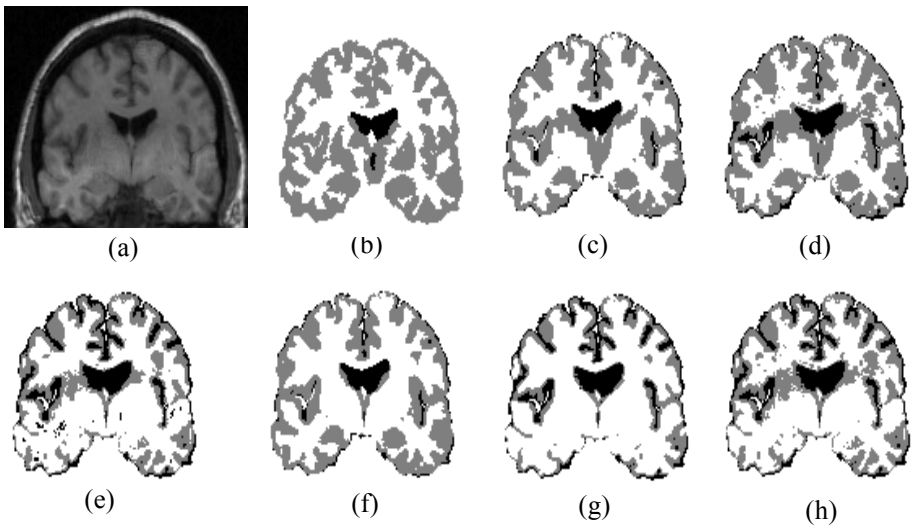

Figure 3.4: Example of segmentation results for each method from IBSR20 dataset (15_3 coronal slice 31): (a) T1-weighted (b) Ground truth (c) Proposed (d) AMS (e) FAST (f) SPM (g) PVC (h) FCM (WM in white, GM in gray and CSF in black).

CHAPTER 4

MRI Whole-Head Tissue Segmentation

This chapter addresses objectives 3 and 4 of this thesis described in chapter 1. It includes three sections. Section 4.1 presents the motivation for developing an automated unsupervised method for whole-head segmentation. The proposed method is presented in section 4.2. An evaluation of the segmentation accuracy of the proposed method is presented in section 4.3.

4.1 Automated head tissue segmentation: Motivation

Segmentation in MR head images can be useful for assigning individual tissues dielectric or biomechanical properties to construct a patient-specific dielectric or biomechanical head model, essential for electromagnetic or biomechanical simulations. Electromagnetic modeling is of importance in applications such as non-invasive EEG source localization in epilepsy patients [19], microwave imaging for stroke detection [20], hyperthermia treatment planning for head and neck tumors [21], the study of electric fields induced by transcranial magnetic stimulation (TMS) [22] and the study of deep brain simulation [23]. Biomechanical modeling is of importance in applications such as brain deformation simulation for image-guided neurosurgery [24] and the study of head trauma in traffic accidents [25].

The accuracy of the MR head tissues segmentation necessarily impacts on the quality and fidelity of electromagnetic or biomechanical modeling. However, the accurate segmentation of head tissues in MR images is a challenging task due to following major reasons: (i) the complexity and variability of the underlying anatomy; (ii) noise; (iii) spatial intensity inhomogeneities; and (iv) the low contrast between the skull, CSF and air in conventionally-used T1-weighted images. This motivates to develop an accurate as well as a fully automatic method for segmenting the head tissues in MR images, important for accurate electromagnetic or biomechanical modeling.

4.2 Proposed whole-head segmentation method

Our proposed method is based on a hierarchical segmentation approach (HSA) incorporating our novel Bayesian-based adaptive mean shift (BAMS) segmentation algorithm

(for more details see paper A). In common with several existing methods [19, 27, 32], the approach includes first dividing the MRI data into brain tissue and non-brain tissue sub-volumes and then independently segmenting each of these into multiple tissue classes. The idea behind this HSA is that the detection of brain and non-brain tissue is a much simpler initial problem than the problem of segmenting the whole head into multiple tissue classes. For example the BET (Brain Extraction Tool, one of the state-of-the-art brain extraction tools) [90] can be employed to robustly obtain a brain-tissue mask whilst simple thresholding and mathematical morphology operations [91, 92] can be employed to obtain a whole-head mask, from which the non-brain tissue mask can then be trivially acquired. What differentiates our method is that a single segmentation approach, BAMS, is applied to segment both the brain tissue and non-brain tissue sub-volumes into multiple tissue classes. The main advantage of BAMS is that it can make use of multiple MRI modalities such as T1-weighted, T2-weighted, and PD.

Hierarchical Segmentation Approach (HSA)

A schematic of the HSA is presented in Fig.4.1. The HSA takes as input a single MR image (T1-weighted) or multi-modal MR images (T1-weighted, T2-weighted and PD) of the whole head. This data can be modeled as a single spatial volume (V) with vector-valued voxels. In the first level of the HSA the T1-weighted data is employed to obtain both a brain mask and a whole head mask. The BET tool is applied to obtain the former and a simple whole head segmentation algorithm (WHSA) is used to obtain the latter. The WHSA comprises two simple steps: (i) Otsu thresholding [91] and (ii) hole filling using morphological reconstruction and 26-connectivity [92]. The set difference between these two masks then yields a mask of the non-brain head tissue. These masks effectively divide the head volume (V) into two disjoint sub-volumes: brain tissue (V_{BT}) and non-brain tissue (V_{NBT}). In the second level of the HSA the multi-tissue segmentation algorithm (MTSA) is employed independently to the brain tissue (V_{BT}) and non-brain tissue (V_{NBT}) volumes to segment them into individual tissue classes V_{BT_1}, V_{BT_2},...and V_{NBT_1}, V_{NBT_2},.... respectively.

4.3 Empirical evaluation of the proposed method

This section summarizes the empirical evaluation, detailed in paper E, of the proposed method, HSA-BAMS. The evaluation was performed relative to a commonly used reference method BET-FAST, and four instantiations of the HSA using both synthetic MRI data (obtained from the Brainweb [51]) and real MRI data from ten subjects. Each HSA instantiation is based on a different multi-tissue segmentation algorithm: the hidden Markov random field model and associated Expectation-Maximization (HMRF-EM) algorithm [62], the adaptive mean shift (AMS) algorithm [41], the improved Fuzzy c-means algorithm with spatial constraints (FCM_S) [93], and the simple k-means clustering algorithm [56]. Hereinafter these instantiations of the HSA are denoted HSA-FAST, HSA-AMS, HSA-FCM_S and HSA-$k$means.

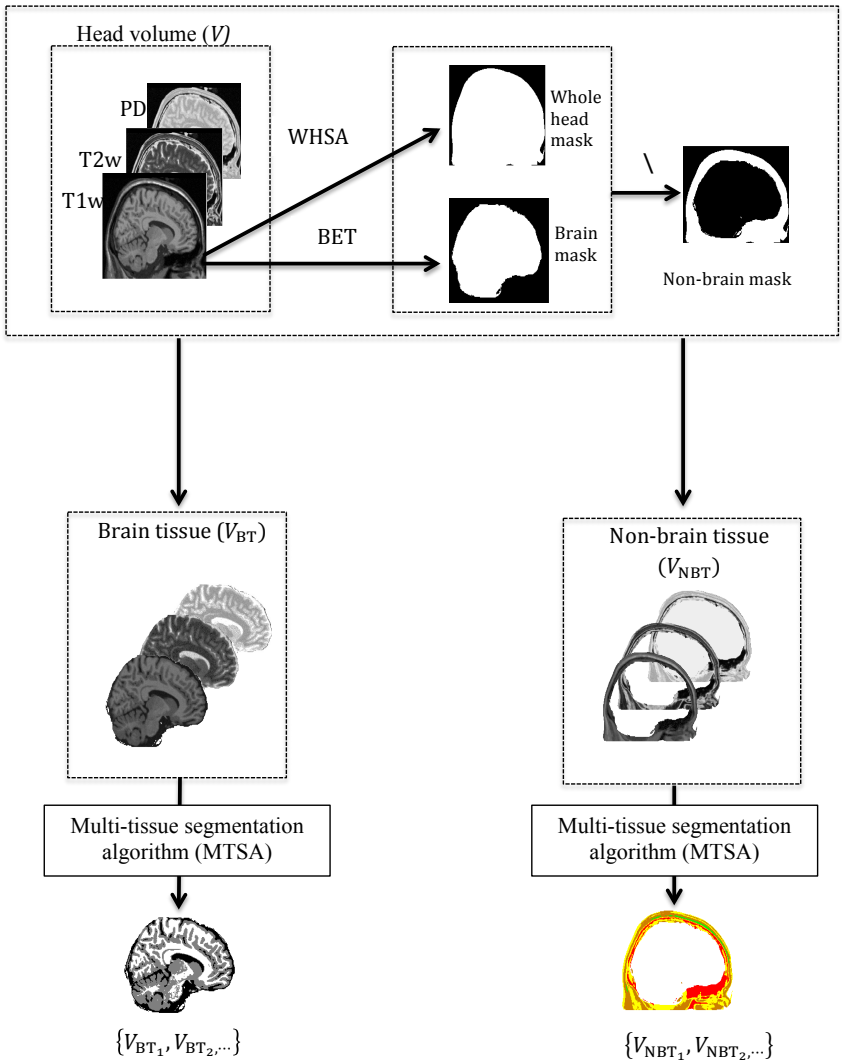

Figure 4.1: Schematic of the proposed hierarchical segmentation approach (HSA) for automated whole head segmentation.

The synthetic data include multiple realizations of four different noise levels, and several realizations of typical noise with a 20% bias field level. For the synthetic MRI data the ground truth was obtained from the nine tissue classes. This was reduced to seven classes by merging tissues with similar conductivity values. Notably, the connective and muscle tissue classes were merged, and the glial matter and GM classes were merged.

For the real data sets, an experienced radio-oncologist manually segmented each subject data into five tissue classes: WM, GM, CSF, skull and skin. This represented a trade-off between the time required to manually segment the images and labeling the essential classes for EEG source localization. The radio-oncologist included fat, muscle, and skin

in the skin class. The manual segmentation took about 170 hours for 200 slices.

Quantitative results

The quantitative performance of the proposed framework and that of each competing method was measured using the Dice index (defined in chapter 3) and the Hausdorff distance [94], which is defined as

$$H = \max\{H_{SG}, H_{GS}\} \tag{4.1}$$

where S and G are two sets of points that belong to the segmentation result and ground truth respectively. $H_{SG} = \max\{d_i^{SG}\}$ is the maximum value of the surface distance (Euclidian distance) of all surface voxels in S and d_i^{SG} represents the minimum distance for the ith surface voxel in S to the set of surface voxels in G. Similarly, $H_{GS} = \max\{d_i^{GS}\}$ is the maximum value of the surface distance of all surface voxels in G and d_i^{GS} represents the minimum distance for the ith surface voxel in G to the set of surface voxels in S.

The quantitative results from paper E for the synthetic dataset with varying noise characteristics are shown in Fig. 2 and 3 respectively and the synthetic data for a particular noise (5%) with 20% bias field is shown in Fig. 4. They show that the segmentation performance of HSA-BAMS is consistently better (higher mean Dice index and lower mean Hausdorff distance) than that of all other instantiations of the HSA as well as the reference method BET-FAST for WM, GM, fat, and muscle tissue especially at higher noise levels (5%, 7%, and 9%). They also show that the segmentation accuracy of the proposed method is comparable (similar mean Dice index and mean Hausdorff distance) to the HSA-AMS and HSA-kmeans methods for the skin and skull tissue.

The quantitative results for the two real datasets (Data set 2 and Data set 3) for each subject are presented in Fig. 6 and 7 respectively. They show that the proposed method HSA-BAMS yields higher segmentation accuracy (higher mean Dice index and lower mean Hausdorff distance) compared to all competing methods for the GM, skin, and skull. However, the performance of the proposed method is comparable (similar Dice index) to all competing methods for the WM (for Data set 2). Moreover, the methods BET-FAST and HSA-FAST have lower Hausdorff distance (H) compared to the proposed method for the CSF (for Data set 3).

Herein, we present in detail, the quantitative results for the real dataset (Data set 4) with eight healthy subjects. The mean Dice index (DI) and mean Hausdorff distance (H) values over the eight subjects for each method and each tissue are shown in Fig. 4.2. They reveal that HSA-BAMS yields higher segmentation accuracy (higher mean Dice index and lower mean Hausdorff distance) than the reference method BET-FAST as well other variants of the HSA for all tissue types.

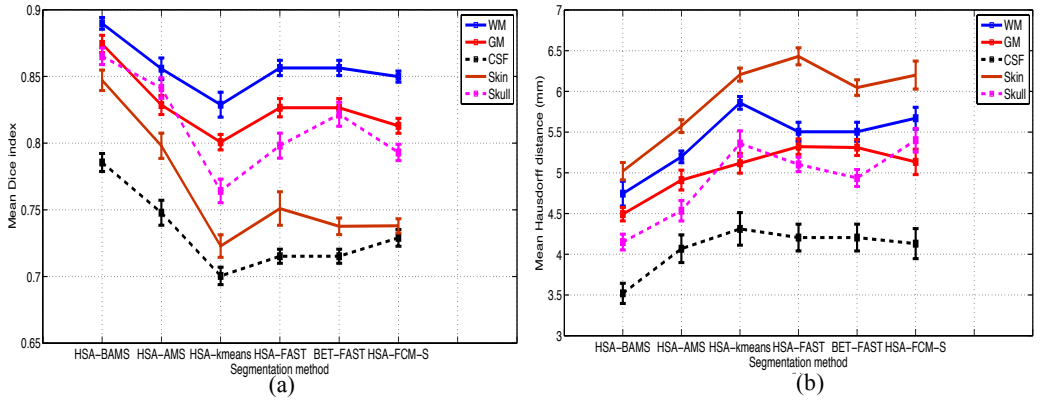

Figure 4.2: Real Dataset: (a) Mean Dice index and (b) Mean Hausdorff distance (mm) over the eight subjects for each tissue and method. In (a) the error bars represent ± 1 standard deviation of the Dice index and in (b) the error bars represent ± 1 standard deviation of the Hausdorff distance.

Qualitative results

An illustration of segmentation for each method for a single sagittal slice (the face region has been excluded) of the subject (IXI040 Guys 0724 [95]) from the real dataset is shown in Fig. 4.3. It can be observed that for the skull tissue, HSA-kmeans, HSA-FCM_S, HSA-FAST and HSA-AMS methods yield higher misclassification whilst for the skin tissue BET-FAST has higher misclassification. For the WM, all the competing methods (HSA-kmeans, HSA-FCM_S, HSA-FAST, HSA-AMS, and BET-FAST) yield higher misclassification compared to the proposed method HSA-BAMS.

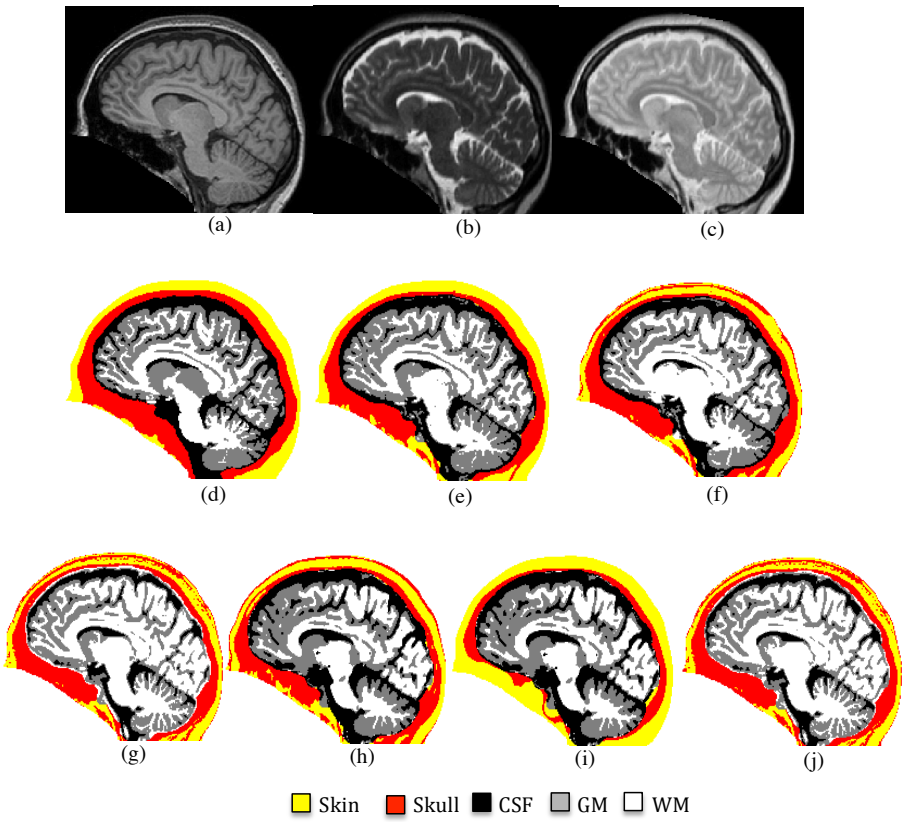

Figure 4.3: Segmentation example for a sagittal slice of the subject from the multi-modal real dataset: (a) T1-weighted image; (b) T2-weighted image; (c) PD image; (d) Ground truth; (e) HSA-BAMS; (f) HSA-AMS; (g) HSA-*k*means; (h) HSA-FAST; (i) BET-FAST; (j) HSA-FCM_S (WM in white, GM in gray, CSF in black, skull in red and skin in yellow).

CHAPTER 5

MRI Whole-Head Tissue Segmentation: Application to EEG Source Localization

This chapter addresses objective 5 of this thesis described in chapter 1. It includes three sections. Section 5.1 presents the motivation for developing an automated unsupervised segmentation method for electroencephalography (EEG) source localization. Section 5.2 describes the EEG source localization problem. An evaluation of the proposed method, described in chapter 4, in the context of EEG source localization is presented in section 5.3.

5.1 Automated head tissue segmentation for EEG source localization: Motivation

Epilepsy is one of the most common neurologic diseases, and is present in up to 1% of the world's population. For epilepsy patients who have not been helped by medication, surgical therapy is often the only feasible intervention.

Source localization of epileptic activity is a tool to delineate cortical areas with abnormal neuronal activity of cells and networks. However, correct and anatomically precise localization of the epileptic focus is essential to decide if resection of brain tissue is possible [96].

Expert manual analysis is considered the gold standard for determining accurate localization of the source of epileptic seizures from electroencephalography (EEG) scalp measurements. Nevertheless, it is a time consuming and laborious process [96]. Several automatic non-invasive EEG source localization methods [97] have been proposed to solve this problem. The accuracy of these methods is not only based on the methods applied to solve the underlying forward and inverse problems [98] but also on the quality and fidelity of the patient-specific head conductivity model used in the forward problem. The construction of a realistic head conductivity model needs accurate segmentation of MR images of the head into tissue types corresponding to different conductivity values. It is usual practice to use five tissue classes: white matter, gray matter, CSF, skull, and skin [27, 99] followed by manual correction for source localization, although improvements in localization accuracy can be obtained with more tissue types [28]. Completely

manual segmentation [26], normally performed by a clinical expert, is the gold standard. However, it is laborious and time-consuming. Two variations that can be found in the literature are interactive segmentation/semi-automatic requiring user intervention [28–31,33], and fully automatic segmentation followed by manual correction [19, 27, 32]. Nevertheless, these approaches are still labor intensive and time consuming. Additionally because user interaction or intervention is needed they are, like completely manual segmentation, subjective and reproducibility is an issue.

Therefore, the limitations of semi-automatic and manual segmentation (outlined above) served as the motivation to develop a fully automatic method from multi-modal MR head images suitable for EEG source localization.

5.2 The EEG Source Localization Problem

EEG source localization is a non-invasive tool applied to locate the source of epileptic seizures in the brain. It involves the solution of two problems: (1) Forward problem that deals with finding the scalp potentials for the given current sources and (2) Inverse problem that deals with estimating the sources to fit with the given potential distributions at the scalp electrodes [27].

5.3 Evaluation of the proposed whole-head tissue segmentation method: EEG source localization accuracy

The accuracy of EEG source localization is based on the quality and fidelity of the patient-specific head conductivity model, which is in turn based on the accuracy of segmentation of the patients head tissues.

Herein, we summarize an indirect empirical evaluation of our proposed segmentation method HSA-BAMS (described in chapter 4) in the context of EEG source localization, presented in paper E. The evaluation was performed relative to the ground truth (GT) and the reference method BET-FAST using synthetic 2D multi-modal MR data with 3% noise level and synthetic EEG, generated for a prescribed source.

In addition, in paper C, the performance of BET-FAST (FSL software) was evaluated relative to the GT using the synthetic MRI data for 3% noise level with 20% bias field for the EEG source localization. In paper D, the GT with five tissues was employed in order to evaluate the modified particle swarm optimization method for EEG source localization of somatosensory evoked potentials in a healthy subjects brain.

In paper E, a 2D GT with seven tissue types for the synthetic multi-modal MRI data, obtained from the BrainWeb, was used and a synthetic EEG was generated by placing a source in the GM of the GT image and calculating the EEG signals from 30 electrodes placed equidistantly on the 2D scalp based on $10/10$ system [27].

To solve the EEG source localization problems, a subtraction method was used for modeling the source (dipole) in the forward problem [100] and a modified particle swarm optimization [27] method was applied to solve the inverse problem.

Quantitative results

The performance of EEG source localization was measured in terms of relative error between the measured and estimated source potential and localization error between the actual source and estimated source distance.
The relative error (RE) is defined as

$$RE = \frac{\|\mathbf{U}_{\text{measured}} - \mathbf{U}_{\text{estimated}}\|}{\|\mathbf{U}_{\text{estimated}}\|} \tag{5.1}$$

where $\mathbf{U}_{\text{measured}}$ is a vector of the measured potential on the head and $\mathbf{U}_{\text{estimated}}$ is a vector of the potential estimated using the simulated source.
The localization error (LE) is defined as

$$LE = \|\mathbf{X}_{\text{true}} - \mathbf{X}_{\text{estimated}}\| \tag{5.2}$$

where $\mathbf{X}_{\text{true}}$ is the real source position and $X_{\text{estimated}}$ is the estimated source position.

The quantitative results, presented in paper E, reveal that the relative error (RE) of the potential and the localization error (LE) for the proposed method HSA-BAMS are 0.01 and 0.00 mm respectively and for the reference method BET-FAST are 0.04 and 4.20 mm respectively. It suggests that using HSA-BAMS leads to better localization accuracy.

Qualitative results

Herein, we discuss the qualitative results of each method, presented in paper E. Fig. 5.1 shows the position of (a) real (simulated) source (in green) (b) estimated source using the proposed method HSA-BAMS (in red) (c) estimated source using the reference method BET-FAST (in blue), superimposed on the ground truth image. It can be seen that the estimated position of the source obtained using HSA-BAMS is in good agreement with the actual position of the source. However, the estimated position of the source obtained using the reference method BET-FAST is not.

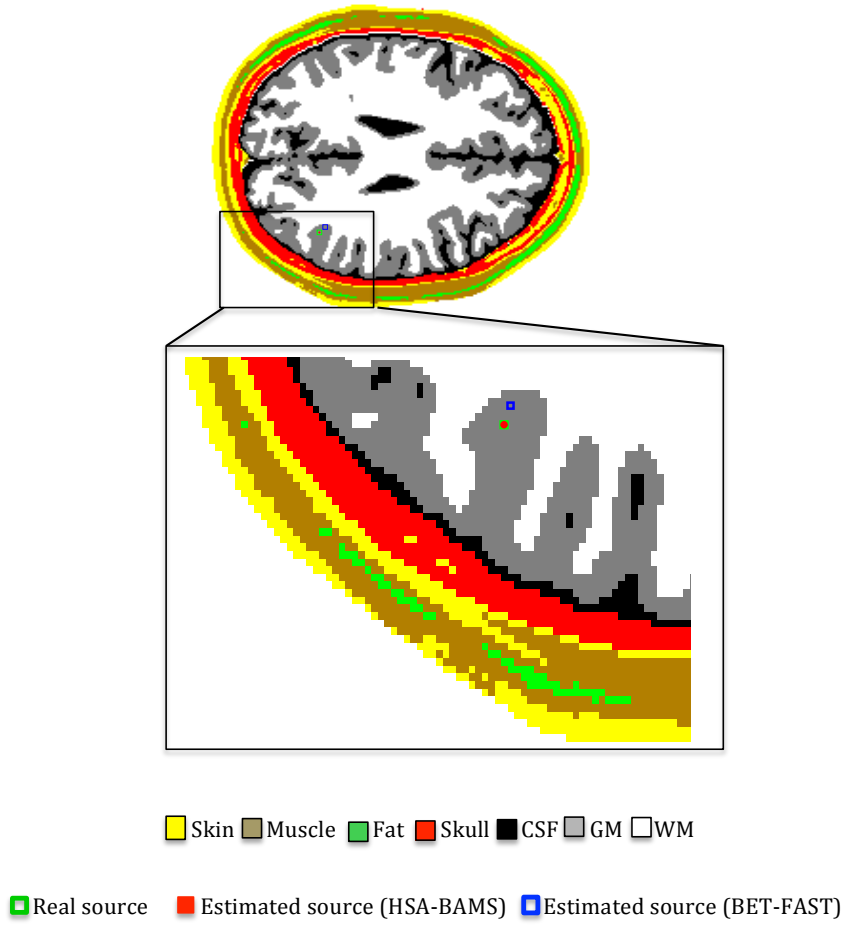

Figure 5.1: EEG source localization results: Ground truth superimposed with the location of the real (simulated) source (green), HSA-BAMS estimated source (red), and BET-FAST estimated source (blue).

CHAPTER 6

MRI Whole-Head Tissue Segmentation: Application to Hemorrhagic Stroke Detection

This chapter addresses objective 6 of this thesis described in chapter 1. It includes two sections. Section 6.1 presents the importance of microwave imaging for stroke detection, including image reconstruction procedure for intracerebral hemorrhage and an overview of automated segmentation methods used for intracerebral detection. An evaluation of segmentation methods, including the proposed method described in chapter 4, in the context of intracerebral hemorrhage detection for a stroke patient is presented in section 6.2.

6.1 Application: Detecting Hemorrhagic Stroke with Microwave-Imaging

Stroke is a neurological disorder that is caused by either a clot blocking an artery or a burst blood vessel causing bleeding inside the cranium. The latter, called intracerebral hemorrhage, is the most common type [101]. Worldwide, each year approximately 15 million people suffer a stroke. A third of these patients don't survive [102].

Computerized Tomography (CT) is presently the gold standard for stroke diagnosis, with MRI frequently being applied when CT fails to give a definitive answer [103]. The major drawback of these imaging modalities is that they are rather bulky. Moreover, they are not portable. Thus, stroke patients have to be brought to the hospital to confirm that they don't have intracerebral hemorrhage before thrombolytic treatment, a treatment employed to dissolve blood clots in the brain, can be provided. Special, large ambulances equipped with CT have been developed to address this problem [104]. Nevertheless, this is an expensive solution and can only be used in heavily populated areas with well developed traffic and telecommunications infrastructure. Ultrasound is a potential future alternative. However, so far this is not applicable for detecting intracerebral hemorrhage [105]. A fast, cost-effective and portable stroke detection imaging system for ordinary ambulances is thus highly desirable.

To achieve this, several microwave systems have been proposed/developed in recent years [20, 35, 36, 106]. The microwave systems proposed in [20, 35, 36], have been used for numerical simulation for stroke detection while the one proposed in [106], has been

applied to clinical measurements from stroke patients.

Microwave imaging uses several microwave antennas placed around the patient's head and measures the amplitude and phase for the propagated signal between all possible pairs of antenna combinations. A single frequency or multiple frequencies in an interval around 1 GHz is often used. The dielectric properties of the brain tissues govern the microwave scattering [107]. The high contrast between blood and brain tissue facilitates the detection of a hemorrhage. Microwave imaging is based on reconstructing dielectric images that can be associated with physiological changes in the brain. To date, 3D reconstruction algorithms typically require several hours for image reconstruction. However, this is not feasible in ambulances where immediate reconstructions are required. It has been proposed [36] that fast reconstruction can be obtained by exploiting *a priori* information about the patient's brain in the healthy state (before stroke onset). In particular, a patient-specific dielectric model of the head is required as starting point; the reconstruction can then be estimated as an update to the prior head model, wherein the measured signals from the patient's head are compared to the corresponding simulations of the head model and changes in the tissue related to the stroke can be localized.

The quality and fidelity of the dielectric head model are essential for the accuracy of image reconstruction. However, the construction of a realistic dielectric head model involves, as a first step, the segmentation of the patient's head tissues from MRI images. The segmentation can then be used to construct a dielectric head model by assigning each tissue type its respective dielectric property (conductivity/permittivity) value. Importantly, the accuracy of MRI tissue segmentation is critical for the construction of a realistic head model required for accurate image reconstruction.

6.1.1 Image reconstruction for intracerebral hemorrhage

Herein, we describe the image reconstruction procedure for intracerebral hemorrhage (shown in Fig. 6.1). The reconstruction involves the following steps:

1. Before the onset of stroke, a patient's MRI data is segmented to generate a patient-specific dielectric head model. The model is then applied for electromagnetic simulations to simulate the scattering parameters: transmission and reflection coefficients (see Fig. 6.1, left).

2. After the onset of stroke, the electromagnetic measurements are performed directly from the patient's head using the microwave antennas surrounding the head (see Fig. 6.1, right).

3. Both measured and simulated scattering parameters are then used in the image reconstruction algorithm, wherein the reconstruction is performed based on the difference between the measured and simulated scattering parameters. The reconstruction represents the change in dielectric properties of the brain tissues associated with intracerebral hemorrhage (see Fig. 6.1, center-bottom).

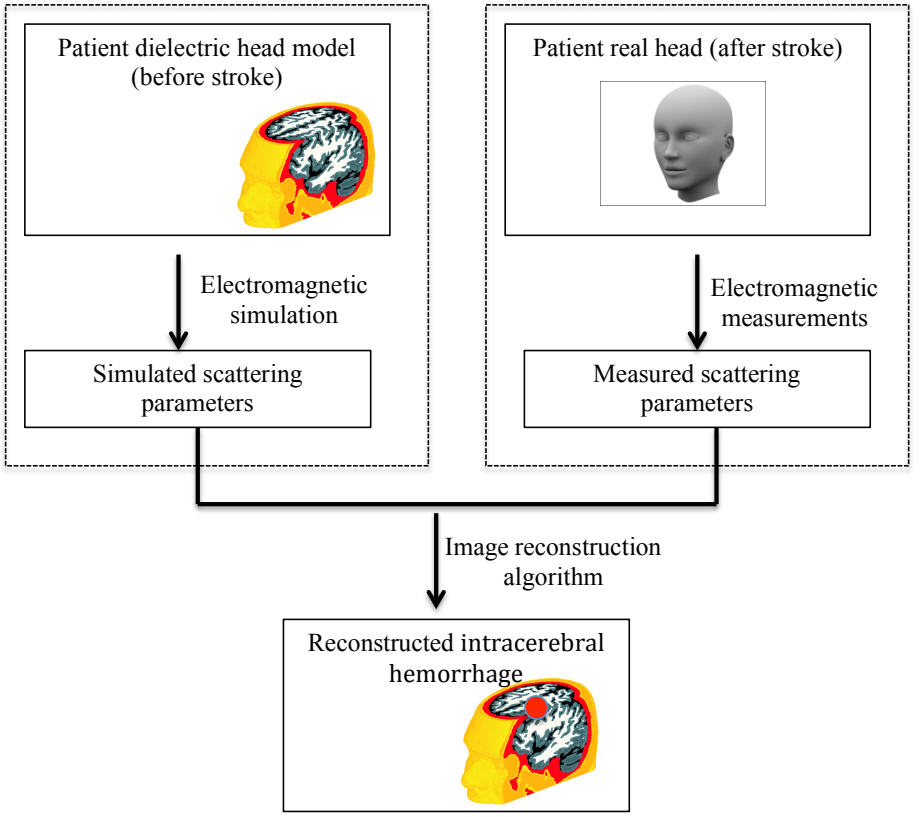

Figure 6.1: Schematic of image reconstruction for intracerebral hemorrhage.

6.2 Evaluation of segmentation methods: Intracerebral hemorrhage detection

This section summarizes the empirical evaluation, detailed in paper F, of automated segmentation methods in the context of intracerebral hemorrhage detection for stroke patient using microwave imaging system.

The evaluation was performed using both synthetic MRI data and real data from four healthy subjects. In the case of the synthetic data the labeled tissues used to generate the MRI data were served as ”ground truth” segmentation. In the case of the real data manual segmentation done by an experienced radio-oncologist, was used as ”ground truth”. The segmentations were done on the full 3D data.

For computational reasons, in this study a 2D dielectric head model was used for electromagnetic simulation and image reconstructions. The 2D model was constructed from a single 2D slice, obtained from the 3D segmented MRI data. Moreover, in this study, we mimic the scenario for real stroke measurements by using simulations of an intracerebral hemorrhage. The dielectric head model without intracerebral hemorrhage was generated

from each automated segmentation methods (described in section 6.2.1) while the head model with simulated intracerebral hemorrhage was generated only from the ground truth. The intracerebral hemorrhage was simulated in the head model by placing a disk of prescribed size in a prescribed position by assigning the pixels the dielectric properties for blood. Eight different hemorrhages were simulated: two different sized disks and four different positions. The radii for the large and small intracerebral hemorrhages were 20 mm and 10 mm (see Fig. 3 in paper F).

The antenna configuration for the microwave imaging system, used in this study for electromagnetic simulations is presented in Fig. 4 (see paper F). The imaging system comprises 20 antennas placed equidistantly around the dielectric head model. The antennas are used both as transmitters and receivers. For each tomographic measurement, one antenna at the time is used as transmitter while the others are used as receivers to measure the scattered signals. This process is continued until all antennas have been used as transmitters and all possible antenna combinations have been measured.

The electromagnetic simulations for the head model without and with hemorrhage were done independently by employing a 2D finite-difference time domain (FDTD) method [108, 109]. The FDTD method was used to simulate the electric fields inside the head model as well as to simulate the scattering parameters from the head model. The electric fields inside and the scattering parameters on the head model without hemorrhage, and the measurements (measured scattering parameters) on the head model with hemorrhage were then used as inputs to the image reconstruction algorithm in order to reconstruct the intracerebral hemorrhage (see Fig. 6.1).

In this study, we applied a fast reconstruction algorithm, which is based on a Born approximation [110] to find the difference between the simulated and measured signals, obtained from the head model without and with hemorrhage respectively, in order to determine the change in dielectric properties of the brain tissues associated with intracerebral hemorrhage.

6.2.1 Automated segmentation methods

We used six unsupervised segmentation methods (including the proposed method presented in chapter 4) for constructing the dielectric head model for use in simulated microwave tomography system for imaging intracerebral hemorrhage for the stroke patients. The segmentation methods comprise the commonly used BET-FAST [62, 90] method, and five variations on a hierarchical segmentation approach (HSA) wherein the MRI data is initially divided into brain and non-brain and then the tissues are independently segmented in each. The detail of HSA is presented in section 4.2 and paper F respectively. Each HSA variant is based on a different multi-tissue segmentation algorithm: FAST [62], Bayesian-based adaptive mean shift (BAMS) [111], adaptive mean shift (AMS) [41], *k*-means method [56], Fuzzy *c*-means method [59]. These variants of the HSA are denoted HSA-FAST, HSA-BAMS (the proposed method presented in chapter 4), HSA-AMS, HSA-*k*means, and HSA-fuzzy *c*means.

Quantitative results

The quantitative evaluation included the measurement of segmentation accuracy over all tissues for a 2D slice, electromagnetic simulation accuracy, and image reconstruction accuracy for simulated intracerebral hemorrhage with two different sizes and four different positions in the brain.

The segmentation accuracy over all tissues, each method and each data was determined in terms of mean Dice score/index [87].

The electromagnetic simulation accuracy was estimated in terms of signal deviation (F). The signal deviation was defined as the sum of squared difference between the scattering signals obtained from the dielectric models with and without intracerebral hemorrhage, respectively. It is given by

$$F = \sum_{k=1}^{N} \sum_{t=1}^{n} \|\mathbf{S}^{'}(k,t) - \mathbf{S}(k,t)\|^2 \tag{6.1}$$

where N is the total number of antennas, n is the total number of signal samples and $\mathbf{S}^{'}(k,t)$ is the tth sample of the scattered signal received from the kth antenna, using the dielectric head model with simulated intracerebral hemorrhage and $\mathbf{S}(k,t)$ is the tth sample of the scattered signal received from the kth antenna, using the dielectric head model without hemorrhage.

The reconstructed image accuracy for both conductivity and permittivity of intracerebral hemorrhage for each dataset and each method was estimated relative to the ground truth in terms of relative error.

The relative error (RE) for the permittivity [108] is given by

$$RE = \frac{\sum_S \|\xi_{GT} - \xi_{ASM}\|}{\sum_S \|\xi_{GT}\|} \tag{6.2}$$

where S is the region of intracerebral hemorrhage being reconstructed, ξ_{GT} represents the permittivity profile of the intracerebral hemorrhage reconstruction using the ground truth, and ξ_{ASM} is the permittivity profile of the intracerebral hemorrhage reconstruction using the automatic segmentation method. The relative error for the conductivity is similarly defined.

Moreover, the degree of overlap between the actual (simulated bleeding in the ground truth brain) and reconstructed intracerebral hemorrhage was computed in terms of Dice score for the image reconstruction accuracy.

The accuracy of electromagnetic microwave simulation is critical for the accurate image reconstruction whilst the accuracy of segmentation is critical for the accurate electromagnetic microwave simulation. In this study we investigated, how the segmentation accuracy influences the electromagnetic microwave simulation accuracy. For this, a relationship between the segmentation accuracy and signal deviation (in logarithmic scale) was evaluated.

In paper F, Fig. 7 shows the combined plots for the mean Dice score over all the tissues and the mean signal deviation over the four different positions for both large and small

intracerebral hemorrhages. Herein we present in detail the results for large intracerebral hemorrhages, shown in Fig. 6.2. The results reveal that relative to the ground truth, the method HSA-BAMS has lowest mean signal deviation and highest mean Dice score compared to all competing methods except for the synthetic data wherein the HSA-BAMS and HSA-AMS are comparable. The results also reveal that the mean signal deviation measured using only the ground truth is negligible compared to that measured using the automated segmentation methods. This indicates that tissue segmentation accuracy influences the simulated scattering signals higher than the intracerebral hemorrhage.

To quantitatively evaluate the accuracy of the reconstructions (shown in figures. 8-12, in paper F), a threshold level *'T'* for both normalized permittivity and conductivity images was chosen to classify the intracerebral hemorrhage and the background. Three different threshold levels (T = 0.6, 0.7, 0.8) were arbitrarily chosen for both permittivity and conductivity images. The permittivity/conductivity values $< T$ were defined as background whilst the permittivity/conductivity values $> T$ were considered as intracerebral hemorrhage in the reconstructed images. The Dice score/index was then calculated to measure the degree of overlap between the actual and reconstructed intracerebral hemorrhage for both permittivity and conductivity.

Fig. 12 in paper F shows the combined plots for the mean Dice score for T = 0.7 and the mean relative error for permittivity for both large and small intracerebral hemorrhage. Herein we present in detail the results for image reconstruction accuracy for large intracerebral hemorrhages, shown in Fig. 6.3. The results for the synthetic data show that relative to the ground truth, the method HSA-BAMS has improved reconstruction accuracy (higher mean Dice score for image reconstruction and mean relative error for permittivity) compared to the competing methods except for the synthetic data, wherein HSA-BAMS and HSA-AMS have a similar reconstruction accuracy (similar mean Dice score for image reconstruction and mean relative error for permittivity). The reason for poorer reconstruction accuracy of other methods for this particular case is that they have higher misclassification of tissues (see Fig. 5 in paper F), especially for the GM and muscle or skin, compared to the HSA-BAMS and HSA-AMS methods.

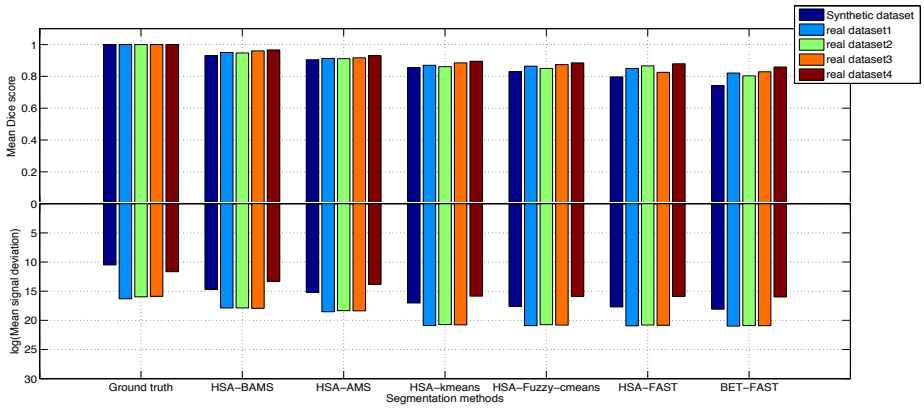

Figure 6.2: Mean Dice score over all the tissues and mean signal deviation (in logarithmic scale) for large intracerebral hemorrhage. In the plot, the results for different segmentation methods are shown along the x-axis, for every method a group of data is shown with different colors, corresponding to different datasets. Along the positive y-axis the bars show the mean Dice score and on the negative y-axis the mean signal deviation in logarithmic scale is shown.

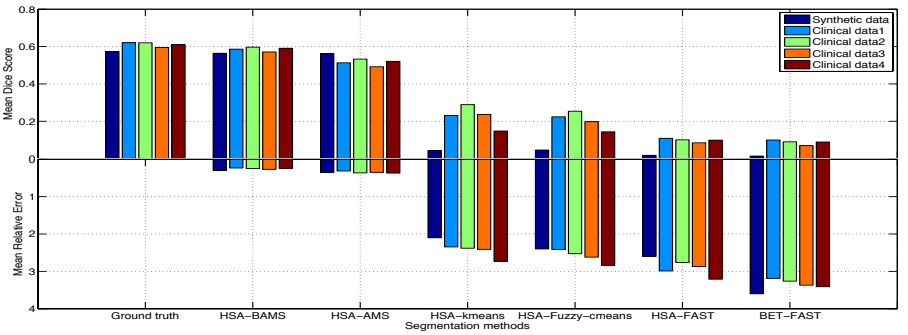

Figure 6.3: Mean Dice score for image reconstruction for $T = 0.7$ and mean relative error for permittivity for large intracerebral hemorrhage. In the plot, the results for different segmentation methods are shown along the x-axis, for every method a group of data is shown with different colors, corresponding to different datasets. Along the positive y-axis the bars show the mean Dice score and on the negative y-axis the mean relative error is shown.

Qualitative results

Sample reconstructions of the permittivity and conductivity profiles for a large intracerebral hemorrhage with radius size of 20 mm from the synthetic dataset are shown in Fig. 6.4 and 6.5 respectively. They show that both segmentation methods HSA-BAMS and HSA-AMS have better reconstruction accuracy for intracerebral hemorrhage compared to the HSA-*k*means, HSA-fuzzy *c*-means, HSA-FAST and the BET-FAST method, and have

a similar reconstruction accuracy compared to the ground truth. These results corroborate the results for the synthetic data presented in Fig. 6.2. In the figures, the contours in the reconstructed images show the structures of the head tissues, wherein the actual intracerebral hemorrhage is shown as a circular contour. The color bar represents the range of intensity for the reconstructed images. In the reconstructed images, the white pixels correspond to background and the yellow and red pixels correspond to the intracerebral hemorrhage.

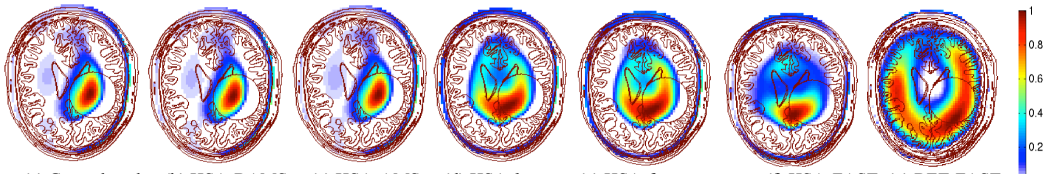

(a) Ground truth (b) HSA-BAMS (c) HSA-AMS (d) HSA-*k*means (e) HSA-fuzzy *c*-means (f) HSA-FAST (g) BET-FAST

Figure 6.4: Reconstruction of the permittivity profile for a large intracerebral hemorrhage with radius size of 20 mm from the synthetic dataset obtained using the different segmentation methods.

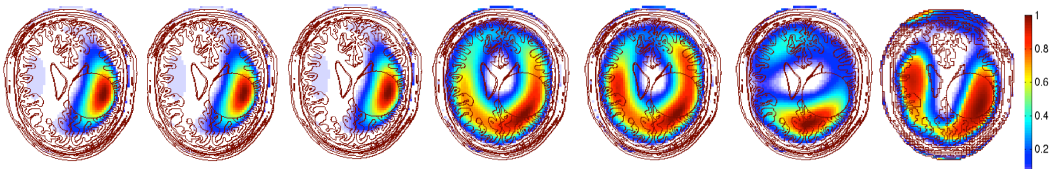

(a) Ground truth (b) HSA-BAMS (c) HSA-AMS (d) HSA-*k*means (e) HSA-fuzzy *c*-means (f) HSA-FAST (g) BET-FAST

Figure 6.5: Reconstruction of the conductivity profile for a large intracerebral hemorrhage with radius size of 20 mm from the synthetic dataset obtained using the different segmentation methods.

CHAPTER 7

Summary of the papers

This chapter presents brief summaries of the enclosed papers, which are categorized into three types; brain segmentation, MRI whole-head segmentation for EEG source localization and MRI whole-head segmentation for intracerebral hemorrhage detection in stroke patients.

7.1 Brain Segmentation

7.1.1 Paper A: A Novel Bayesian Approach to Adaptive Mean Shift Segmentation of Brain Images

In this paper, we propose a novel adaptive mean shift algorithm for the segmentation of multi-modal MR images of the brain into three tissue types: white matter (WM), gray matter (GM) and cerebrospinal fluid (CSF). The novelty lies in the algorithm for the estimation of adaptive bandwidth of the kernel. The algorithm is called a Bayesian adaptive mean shift (BAMS) wherein the Bayesian approach is employed for adaptive bandwidth estimation. The approach involves fitting the Gamma distribution probability density function to the local variances of N sets of neighborhoods around the current feature point. The accuracy of the proposed algorithm BAMS was evaluated relative to another adaptive mean shift algorithm that is based on the k nearest neighbors (kNN) bandwidth estimator as well as several other existing methods. The segmentation experiments were performed on both multi-modal synthetic (T1-, T2-, PD-weighted) MRI data with different levels of noise and real T1-weighted MRI data with varying levels of spatial intensity inhomogeneities. The performance of the segmentation methods was measured using the Dice and Tanimoto coefficient. The results demonstrate the efficacy and accuracy of the proposed BAMS algorithm and that it performs well compared to the competing methods especially when the noise and spatial intensity inhomogeneities are high.

7.1.2 Paper B: Automated MRI Brain Tissue Segmentation based on Mean Shift and Fuzzy *C*-Means using *a Priori* Tissue Probability Maps

In this paper, we propose a novel fully automatic unsupervised segmentation framework for the segmentation of three tissue types from the MRI brain images. The framework is based on the Bayesian-based adaptive mean shift to initially divide the brain into a number of clusters and the fuzzy c-means algorithm, wherein the *a priori* spatial tissue probability maps are incorporated, to classify the resulting clusters into WM, GM and CSF tissue. The segmentation accuracy of the proposed framework was evaluated relative to three widely used brain segmentation toolboxes: FAST, SPM, and PVC and the adaptive mean shift (AMS) and classical fuzzy c-means (FCM) methods. The evaluation was done on a synthetic T1-weighted MR image for four different noise levels (3%, 5%, 7%, 9%) with two different spatial intensity inhomogeneity levels (20%, 40%), obtained from the BrainWeb database as well as on 38 real T1-weighted MR images, obtained from the IBSR repository. The experimental results, especially for the real datasets reveal that for some cases, the proposed framework has less segmentation accuracy for some tissue compared to the competing methods. However, overall the performance of the proposed framework is better compared to all competing methods. Moreover, incorporation of *a priori* spatial tissue probability maps in the proposed framework makes the tissue segmentation objective and reproducible.

7.2 MRI Whole-Head Segmentation: EEG Source Localization

7.2.1 Paper C: Investigation of Brain Tissue Segmentation Error and Its Effect on EEG Source Localization

In this paper, the segmentation performance of two widely used brain segmentation tools: FSL (FAST) and FreeSurfer were evaluated relative to the ground truth (gold standard segmentation). The evaluation was performed using the synthetic MRI data with varying noise and bias field levels, obtained from the BrainWeb. The segmentation results show that FSL is more robust compared to FreeSurfer, especially for the CSF, one of the most important tissues for EEG source localization. Based on the FSL segmentation, an electro-conductivity head model was then constructed in order to investigate the effects of brain tissue segmentation on EEG source localization. A combination of the subtraction method and modified particle swarm optimization method was applied to solve the EEG source localization problems. The experimental results show that the source estimated using the FSL based electro-conductivity model has a 12 mm localization error in the z-direction of the estimated source.

7.2.2 Paper D: Particle Swarm Optimization Applied to EEG Source Localization of Somatosensory Evoked Potentials

In this paper, a modified particle swarm optimization method was applied for EEG source localization of somatosensory evoked potentials in a healthy subject's brain. This paper provides an extension of the work presented in paper C, wherein it is shown that the widely used brain segmentation tool: FSL has high misclassifications of skull and CSF tissue. This might cause significant errors in source localization results. Herein, manual segmentation of T1-weighted MRI data of the healthy subject, done by a radiologist, was employed. The segmentation was then applied to construct a conductivity model for source localization of somatosensory evoked potentials. The experimental results show that using the expert manual segmentation of tissues, the modified particle swarm optimization method yields the accurate source localization of somatosensory evoked potentials in the healthy subject's brain with respect to the clinical expert determined source localization as well as to the exhaustive search source localization method.

7.2.3 Paper E: Unsupervised Segmentation of Head Tissues from Multi-modal MR Images for EEG Source Localization

In this paper, we propose and present a new fully automatic unsupervised method for head tissue segmentation from multi-modal MR images for use in the construction of a patient specific model for EEG source localization. The method is based on a hierarchical segmentation approach (HSA), wherein the MRI data are initially divided into brain tissue and non-brain tissue sub-volumes and then each sub-volume is independently segmented into multiple tissue classes. What differentiates our method is that a single segmentation approach, Bayesian adaptive mean shift (BAMS), is used to segment both the brain tissue and non-brain tissue sub-volumes into multiple tissue classes. Several evaluations of the performance of the proposed method and of reference as well as variant methods were also presented. This included direct evaluation in terms of segmentation accuracy and indirect evaluation in terms of EEG source localization accuracy. The segmentation results show that compared to the competing methods, the proposed method is more tolerant to the noise and the bias field for the synthetic data. For the real datasets, the proposed method also has higher segmentation accuracy for the tissue types essential for the EEG source localization compared to each competing method. Moreover, multiple comparisons statistical tests (consisting of several McNemar tests) also show that the proposed method HSA-BAMS performs differently ($p\text{-}values < 0.016$) to all other methods for each tissue type, especially for the real datasets. For the case of EEG source localization, the results show that the proposed method yields a better performance compared to the reference method BET-FAST, commonly used for the construction of a realistic head model for EEG source localization. Overall the experimental results suggest that the proposed method HSA-BAMS can be used as a surrogate for the reference method BET-FAST as well as manual segmentation for the construction of patient-specific head models for EEG source localization.

7.3 MRI Whole-Head Segmentation: Intracerebral Hemorrhage Detection in Stroke Patients

7.3.1 Paper F: A Comparative Study of Automated Segmentation Methods for Use in a Microwave Tomography System for Imaging Intracerebral Hemorrhage in Stroke Patients

In this paper, we present an evaluation of several unsupervised segmentation methods in the context of intracerebral hemorrhage detection in stroke patients using a microwave imaging system. The evaluation was performed using both synthetic MRI data and real data from four healthy subjects. In the case of the synthetic data the labeled tissues used to generate the MRI data were used as ”ground truth” segmentation. In the case of the real data expert manual segmentation was served as ”ground truth”. The segmentations were done on the full 3D data, whereas the electromagnetic evaluation was performed using a 2D slice. For evaluation of methods, we calculated the segmentation accuracy over the tissues relative to the ground truth. We also evaluated the effect caused by misclassification of tissue on the electromagnetic wave propagation through the head and on the reconstruction accuracy of hemorrhage. The segmentation accuracy was measured in terms of the degree of overlap (Dice score) between the ground truth and the method segmentation. The electromagnetic simulation accuracy was measured in terms of signal deviation relative to the simulation based on the ground truth. Finally, the image reconstruction accuracy was measured in terms of the Dice score, the relative error of dielectric properties, and visual assessment between true and reconstructed intracerebral hemorrhage. The experimental results reveal that accurate image reconstruction for the intracerebral hemorrhage in the subject's brain can be achieved by accurate segmentation of tissues in the MRI data. They also indicate that accurate automated segmentation (in this study, particularly HSA-BAMS) can be applied in lieu of manual segmentation and can assist in fast diagnosing the intracerebral hemorrhage in stroke patients using the microwave imaging system.

CHAPTER 8

Conclusions and Outlook

In this chapter our contributions are summarized and directions for future work are discussed.

8.1 Conclusions

The contributions of this thesis are four-fold. First, we studied the brain segmentation problem for three tissue types: WM, GM and CSF in MR images, wherein accurate segmentation is a challenging task because of the two major artifacts: noise and spatial intensity inhomogeneity (bias field). In chapter 3, we presented an unsupervised segmentation framework, which is a combination of Bayesian adaptive mean shift, *a priori* spatial tissues probability maps and the fuzzy *c*-means algorithm. The important characteristic of the proposed framework is that it provides the segmentation of tissue by taking both the spatial and intensity domain and the *a priori* spatial information using probabilistic atlas into account. This makes the proposed method more robust to noise and spatial intensity inhomogeneity. Overall the experimental results showed that the proposed framework exhibited a higher degree of segmentation accuracy in segmenting both synthetic and 38 real T1-weighted MR images compared to the competing methods. However, over all the subjects for each real dataset, the proposed framework has decreased in performance for the CSF compared to the WM and GM.

Second, we studied the whole-head segmentation problem in the multi-modal MR images for use in the construction of a patient specific dielectric model. In chapter 4, we proposed an automated unsupervised MRI whole-head tissue segmentation method for use in biomechanical or electromagnetic modeling. The method is based on a hierarchical segmentation approach (HSA) incorporating the Bayesian-based adaptive mean-shift (BAMS), wherein the MRI data is first partitioned into brain tissue and non-brain tissue sub-volumes and then each sub-volume is independently segmented.

Third, we studied the influence of MRI head tissue segmentation on the accuracy of EEG source localization. In chapter 5, the proposed whole-head tissue segmentation method HSA-BAMS is evaluated for the EEG source localization. The experimental results demonstrated the accuracy of the proposed method, and that it is more suitable than the reference method BET-FAST commonly used for constructing the realistic head con-

ductivity model for EEG source localization.

Fourth, we studied the influence of MRI head tissue segmentation on the accuracy of image reconstruction for intracerebral hemorrhage detection in stroke patients using a microwave imaging system. In chapter 6, we presented an evaluation of the proposed whole-head tissue segmentation method HSA-BAMS for use in constructing a dielectric head model for imaging intracerebral hemorrhage in stroke patients using a simulated microwave imaging system. The experimental results demonstrated that the proposed method yields a higher image reconstruction accuracy for intracerebral hemorrhage compared to the existing methods. The results also revealed that accurate automated segmentation can be used in lieu of manual segmentation for accurate image reconstruction and can assist in real time stroke detection in the patient's brain using the microwave imaging system.

8.2 Future work

Based on the studies presented in this thesis, the following possibilities can be explored in future research.

- The proposed framework for brain segmentation, presented in chapter 3, can be applied for segmenting MR images containing abnormal brain tissues like sclerotic lesions and tumors. This will likely require additional MRI modalities and possibly also imaging modalities. These can be readily accommodated in the proposed method.

- The robustness of the proposed method, presented in chapter 4, can be investigated for real time diagnosis of stroke patients in the ambulance equipped with a microwave imaging system.

- The proposed method, presented in chapter 4, can also be investigated for hyperthermia treatment planning for head and neck tumors, wherein the accurate segmentation for tumors and tissues surrounding the tumors are crucial for accurate treatment.

- The proposed framework, presented in chapter 3, can be investigated for simultaneous tissue segmentation and bias field estimation of MR images. This can be achieved by extending the fuzzy c-means objective function (Eq.2.15) for bias field estimation [112].

- T1- and T2-weighted MR images contain low contrast between the air and the skull tissue, which may cause misclassification of the skull. One potential solution to this problem is to incorporate *a priori* anatomical information; e.g. using a probabilistic atlas. This can be investigated for the proposed method, presented in chapter 4.

- It can also be possible to investigate other contemporary segmentation techniques such as multi-atlas segmentation methods for EEG source localization and stroke

detection in the patient's brain. Multi-atlas yields a better tissue segmentation for the brain datasets with large anatomical variations than a single atlas [113].

Bibliography

[1] O. F. Erondu. *Medical Imaging*. InTech, 2011.

[2] W. R. Hendee and E. R. Ritenour. *Medical Imaging Physics*. Wiley-Liss, 2002.

[3] C. Guy and D. Ffytche. *An Introduction to The Principles of Medical Imaging*. Imperial College Press, 2008.

[4] B. L. Hart, E. C. Benzel, and C. C. Ford. *Fundamentals of Neuroimaging*. W. B. Saunders, 1997.

[5] B. Hüsing, L. Jäncke, and B. Tag. *Impact Assessment of Neuroimaging*. Institute for Biomedical Engineering, University of Zurich and ETHZ, Zurich, Switzerland, 2005.

[6] B. Crosson, A. Ford, K. M. McGregor, M. Meinzer, S. Cheshkov, X. Li, D. Walker-Batson, and R. W. Briggs. Functional imaging and related techniques: An introduction for rehabilitation researchers. *J. Rehabil. Res. Dev.*, 47(2):vii–xxxiv, 2010.

[7] D. L. Bailey, D. W. Townsend, P. E. Valk, and M. N. Maisey. *Positron Emission Tomography: Basic Sciences*. Secaucus, NJ: Springer-Verlag, 2005.

[8] S. A. Huettel, A. W. Song, and G. McCarthy. *Functional Magnetic Resonance Imaging*. Massachusetts: Sinauer, 2nd edition, 2009.

[9] E. S. Schwartz, D. J. Dlugos, P. B. Storm, J. Dell, R. Magee, T. P. Flynn, D. M. Zarnow, R. A. Zimmerman, and T. P. Roberts. Magnetoencephalography for pediatric epilepsy: how we do it. *American Journal of Neuroradiology*, 29(5):832–837, 2008.

[10] E. B. Swartz. The advantages of digital over analog recording techniques. *Electroencephalography and Clinical Neurophysiology*, 106(2):113–7, 1998.

[11] G. W. Small. *Chapter 86: Structural and functional brain imaging of Alzheimer disease, Neuropsychopharmacology: The Fifth Generation of Progress*. Lippincott Williams Wilkins, 2002.

[12] G. T. Herman. *Fundamentals of computerized tomography: Image reconstruction from projection*. Springer, 2009.

[13] J. B. Jr Ball and M. L. Pensak. Fundamentals of Magnetic Resonance Imaging. *American Journal of Otolaryngology*, 8:81–85, 1987.

[14] G. Zhai, W. Lin, K. Wilber, G. Gerig, and J. H. Gilmore. Comparison of regional white matter diffusion in healthy neonates and adults using a 3T head-only MR scanner. *Radiology*, 229:673–681, 2003.

[15] J. Gilmore, G. Zhai, K. Wilber, J. Smith, and W. Lin. 3T magnetic resonance imaging of the brain in newborns. *Psychiatry Research Neuroimaging*, 132:81–85, 2004.

[16] W. Minjie. *Registration and segmentation of brain MR images from elderly individuals*. PhD thesis, University of Pittsburgh, 2009.

[17] X. Han and B. Fischl. Atlas renormalization for improved brain MR image segmentation across scanner platforms. *IEEE Trans. Med. Imaging*, 26(4):479–486, 2007.

[18] H. Greenspan, A. Ruf, and J. Goldberger. Constrained Gaussian mixture model framework for automatic segmentation of MR brain images. *IEEE Trans. Med. Imaging*, 25(9):1233–1245, 2006.

[19] M. Rullmann, A. Anwander, M. Dannhauer, S. Warfield, F. Duffy, and C. Wolter. EEG source analysis of epileptiform activity using a 1 mm anisotropic hexahedra finite element head model. *NeuroImage*, 44(2):399–410, 2009.

[20] D. Ireland and M. Bialkowski. Microwave head imaging for stroke detection. *Progress in Electromagnetics Research M*, 21:163–175, 2011.

[21] V. Fortunati, R. F. Verhaart, F. van der Lijin, W. J. Niessen, J. F. Veenland, M. M. Paulides, and T. van Walsum. Hyperthermia critical tissues automatic segmentation of head and neck CT images using atlas registration and graphcuts. *In Proceedings of International Symposium on Biomedical Imaging (ISBI)*, pages 1683–1686, 2012.

[22] A. Opitz, M. Windhoff, R. Heidemann, R. Turner, and A. Thielscher. How the brain tissue shapes the electric field induced by transcranial magnetic simulation. *NeuroImage*, 58:849–859, 2011.

[23] K. Wårdell, E. Diczfalusy, and M. Åström. Patient specific modeling and simulation of deep brain stimulation. *In Patient Specific Modeling in Tomorrow's Medicine*, pages 357–378, 2011.

[24] O. Clatz, H. Delingette, E. Bardinet, D. Dormont, and N. Ayache. Patient specific biomedical model of the brain: application to Parkinson's disease procedure. *In Proceedings of the International Conference on Surgery Simulation and Soft Tissue*, pages 321–331, 2003.

[25] K. Voo, S. Kumaresan, A. F. Pintar, N. Yoganandan, and A. Sances Jr. Finite element models of the human head. *Med. Biol. Eng. Comput.*, 34:375–381, 1996.

[26] Y. Shirvany, Q. Mahmood, F. Edelvik, M. Persson, A. Hedström, and S. Jakobsson. Particle swarm optimization applied to EEG source localization of somatosensory evoked potentials. *IEEE Transactions on Neural Systems and Rehabilitation Engineering*, 22(1):11–20, 2013.

[27] Y. Shirvany, F. Edelvik, S. Jakobsson, A. Hedström, Q. Mahmood, A. Chodorowski, and M. Persson. Non-invasive EEG source localization with Particle Swarm Optimization: Clinical Test. *In Proceedings of Engineering in Medicine and Biology Society (EMBC)*, pages 6232–6235, 2012.

[28] C. Ramon, P. H. Schimpf, and J. Haueisen. Influence of head models on EEG source localizations and inverse source localizations. *BioMedical Engineering OnLine*, pages 5–10, 2006.

[29] B. Yvert, O. Bertrand, and J. Echallier. Improved forward EEG calculations using local mesh refinement of realistic head geometries. *Electroencephalography and Clinical Neurophysiology*, 5:381–392, 1995.

[30] T. Heinonen and H. Eskola. Segmentation of T1 MR scans for reconstruction of resistive head models. *Computer Methods and Programs in Biomedicine*, 54:173–81, 1997.

[31] T. Heinonen, P. Dastidarb, F. Frey, and H. Eskola. Applications of MR image segmentation. *International Journal of Bioelectromagnetism*, 1:5–39, 1999.

[32] B. Lanfer, M. Scherg, M. Dannhauer, T. R. Knösche, M. Burger, and C. H. Wolters. Influences of skull segmentation inaccuracies on EEG source analysis. *NeuroImage*, 62:418–31, 2006.

[33] Z. A. Acar and S. Makeig. Neuroelectromagnetic forward modeling toolbox. *Journal of Neuroscience Methods*, 190:258–270, 2010.

[34] A. Datta, J. M. Baker, M. Bikson, and J. Fridriksson. Individualized model predicts brain current flow during transcranial direct-current stimulation treatment in responsive stroke patient. *Brain Stimul.*, 4(3):169–174, 2011.

[35] R. Scapaticci, L. Di Donato, I. Catapano, and L. Crocco. A feasibility study on microwave imaging for brain stroke monitoring. *Progress in Electromagnetics Research B*, 40:305–324, 2012.

[36] N. Irishina and A. Torrente. Brain stroke detection by microwaves using prior information from clinical databases. *Abstract and Applied Analysis*, 2013:1–8, 2013.

[37] C Haegelen, D. García-Lorenzo, F. Le Jeune, J. Péron, B. Gibaud, L. Riffaud, G. Brassier, C. Barillot, M. Vérin, and X. Morandi. SPECT and PET analysis of subthalamic stimulation in Parkinson's disease: analysis using a manual segmentation. *Journal of Neurology*, 257:375–382, 2010.

[38] L. P. Clarke, R. P. Velthuizen, M. A. Camacho, J. J. Heine, M. Vaidyanathan, L. O. Hall, R. W. Thatcher, and M. L. Silbiger. MRI segmentation: Methods and applications. *Magnetic Resonance Imaging*, 13:343–368, 1995.

[39] L. P. Clarke, R. P. Velthuizen, S. Phuphanich, J. D. Schellenberg, J. A. Arrington, and M. Silbiger. MRI: Stability of three supervised segmentation techniques. *Magnetic Resonance Imaging*, 11:95–101, 1993.

[40] M. Cabezas, A. Oliver, X. Lladó, J. Freixenet, and M. B. Cuadra. A review of atlas-based segmentation for magnetic resonance brain images. *Computer Methods and Programs in Biomedicine*, 104(3):158–77, 2011.

[41] A. Mayer and H. Greenspan. An adaptive mean-shift framework for MRI brain segmentation. *IEEE Trans. Med. Imaging*, 28(8):1238–1249, 2009.

[42] F. Wang, D. Shen, P. Yan, and K. Suzuki. Volumetric segmentation of key fetal brain structures in 3D ultrasound. *Medical Image Computing and Computer Assisted Intervention (MICCAI) 2013, LNCS*, 8184:25–32, 2013.

[43] A. Brodal. *Neurological Anatomy in Relation to Clinical Medicine*. Oxford Univ. Press, New York, 3rd edition, 1981.

[44] C. R. Noback, N. L. Strominger, R. J. Demarest, and D. A. Ruggiero. *The Human Nervous System Structure and Function*. Humana Press Inc., Totowa, New Jersey, 6th edition, 2005.

[45] E. A. Kandel, J. Schwartz, and T. M. Jessell. *Principles of Neural Science*. McGraw-Hill Companies, 4th edition, 2000.

[46] D. W. McRobbie, E. A. Moore, M. J. Graves, and M. R. Prince. *MRI: From picture to proton*. Cambridge, 2nd edition, 2007.

[47] R. R. Ernst, G. Bodenhausen, and A. Wokaun. *Principles of Nuclear Magnetic Resonance in one and two dimensions*. Oxford University Press, USA, 1990.

[48] P. T. Callaghan. *Principles of Nuclear Magnetic Resonance Microscopy*. Oxford University Press, USA, 1993.

[49] R. A. Pooley. Fundamental physics of MR imaging. *RadioGraphics*, 25:1087–1099, 2005.

[50] F. Bloch. Nuclear induction. *Physical Review*, 70:460–473, 1946.

[51] Brainweb:Simulated Brain Database. `http://brainweb.bic.mni.mcgill.ca/brainweb/`.

[52] S. Aja-Fernandez, C. Alberola-Lopez, and C. F. Westin. Noise and signal estimation in magnitude MRI and Rician distributed images: a LMMSE approach. *IEEE Transactions on Image Processing*, 17:1383–1398, 2008.

[53] M. A. Balafar, A. R. Ramli, M. I. Saripan, and S. Mashohor. Review of brain MRI image segmentation methods. *Artif. Intell. Rev.*, 33(3):261–274, 2010.

[54] K. Fukunaga and L. D. Hostetler. The Estimation of the Gradient of a Density Function, with Applications in Pattern Recognition. *IEEE Transactions on Information Theory*, 21:32–40, 1975.

[55] D. Comaniciu and P. Meer. Mean Shift: A robust approach toward feature space analysis. *IEEE Trans. Pattern Anal. Mach. Intell.*, 24(5):603–619, 2002.

[56] J. B. MacQueen. Some methods for classification and analysis of multivariate observations. *In Proceedings of 5th Berkeley Symposium on Mathematical Statistics and Probability*, pages 281–297, 1967.

[57] A. K. Jain. Data clustering: 50 years beyond k-means. *Pattern Recognition Letters*, 31:651–666, 2010.

[58] J. C. Dunn. A fuzzy relative of the isodata process and its use in detecting compact well-separated clusters. *Journal of Cybernetics*, 3:32–57, 1973.

[59] J. C. Bezdek. *Pattern Recognition with Fuzzy Objective Function Algoritms*. Plenum Press, New York, 1981.

[60] M. A. Balafar. Gaussian mixture model based segmentation methods for brain MRI images. *Artif. Intell. Rev.*, 41:429–439, 2014.

[61] A. P. Dempster, N. M. Laird, and D. B. Rubin. Maximum likelihood from incomplete data via the EM algorithm. *Journal of the Royal Statistical Society*, 39:1–38, 1977.

[62] Y. Zhang, M. Brady, and S. Smith. Segmentation of brain MR images through a Hidden Markov Random Field Model and the Expectation Maximization algorithm. *IEEE Trans. Med. Imaging*, 20(1):45–57, 2001.

[63] J. Besag. On the statistical analysis of dirty pictures (with discussion). *Journal of Royal Statist. Soc. B*, 48:259–302, 1986.

[64] J. Ashburner. SPM: a history. *NeuroImage*, 62:791–800, 2012.

[65] Statistical parametric mapping (SPM). `http://www.fil.ion.ucl.ac.uk/spm/`.

[66] D. W. Shattuck, S. R. Sandor-Leahy, K. A. Schaper, D. A. Rottenberg, and R. M. Leahy. Magnetic resonance image tissue classification using a partial volume model. *NeuroImage*, 13:856–876, 2001.

[67] A. M. Dale, B. Fischl, and M. I. Sereno. Cortical surface based analysis I. segmentation and surface reconstruction. *NeuroImage*, 9:179–194, 1999.

[68] J. C. Bezdek, L. O. Hall, and L. P. Clarke. Review of MR image segmentation techniques using pattern recognition. *Med. Phys.*, 20:1033–1048, 1993.

[69] A. Zijdenbos, R. Forghani, and A. Evans. Automatic quantification of MS lesions in 3D MRI brain data sets: Validation of insect. *In Proceedings of Medical Image Computing and Computer Assisted Intervention (MICCAI)*, pages 439–448, 1998.

[70] C. Cocosco, A. Zijdenbos, and A. Evans. A fully automatic and robust brain MRI tissue classification method. *Med. Image Anal.*, 7:513–527, 2003.

[71] R. Cárdenes, S. K. Warfield, E. M. Macías, J. A. Santana, and J. Ruiz-Alzola. An efficient algorithm for multiple sclerosis segmentation from brain MRI. *Int. Workshop Comput. Aided Syst. Theory (EUROCAST)*, pages 542–551, 2003.

[72] A. Akselrod-Ballin, M. Galun, J. M. Gomori, R. Basri, and A. Brandt. Atlas guided identification of brain structures by combining 3D segmentation and SVM classification. *In Proceedings of Medical Image Computing and Computer Assisted Intervention (MICCAI)*, pages 209–216, 2006.

[73] A. van Opbroek, M. Arfan Ikram, M. W. Vernooij, and M. de Bruijne. Supervised image segmentation across scanner protocols: A transfer learning approach. *MLMI, Lecture Notes in Computer Science*, 7588:160–167, 2012.

[74] K. Van Leemput, F. Maes, D. Vandeurmeulen, and P. Suetens. Automated model-based tissue classification of MR images of the brain. *IEEE Trans. Med. Imaging*, 18(10):897–908, 1999.

[75] K. Van Leemput, F. Maes, D. Vandermeulen, and P. Suetens. A unifying framework for partial volume segmentation of brain MR images. *IEEE Trans. Med. Imaging*, 22:105–119, 2003.

[76] G. Dugas-Phocion, M. A. González Ballester, G. Malandain, C. Lebrun, and N. Ayache. Improved EM-based tissue segmentation and partial volume effect quantification in multi-sequence brain MRI. *In Proceedings of Medical Image Computing and Computer Assisted Intervention (MICCAI)*, pages 26–33, 2004.

[77] J. L. Marroquin, B. C. Vemuri, S. Botello, and F. Calderon. An accurate and efficient Bayesian method for automatic segmentation of brain MRI. *IEEE Trans. Med. Imaging*, 21(8):934–944, 2002.

[78] D. W. Shattuck, S. R. Sandor-Leahy, K. A. Schaper, D. A. Rottenberg, and R. M. Leahy. Magnetic resonance image tissue classification using a partial volume model. *NeuroImage*, 13(856-876), 2001.

[79] J. Tohka, I. D. Dinov, D. W. Shattuck, and A. W. Toga. Brain MRI tissue classification based on local Markov Random Fields. *Magnetic Resonance Imaging*, 28:557–573, 2010.

[80] B. Scherrer, F. Forbes, C. Garbay, and M. Dojat. Distributed local MRF models for tissue and structure brain segmentation. *IEEE Trans. Med. Imaging*, 28:1278–1295, 2009.

[81] D. Comaniciu. An algorithm for data-driven bandwidth selection. *IEEE Trans. Pattern Anal. Mach. Intell.*, 25:281–288, 2003.

[82] B. Georgescu, I. Shimshoni, and P. Meer. Mean-shift based clustering in high dimensions: A texture classification example. *In Proceedings of ICCV*, 91(433):456–463, 2003.

[83] A. G. Bors and N. Nasios. Kernel bandwidth estimation for nonparametric modeling. *IEEE Transactions on Systems, Man, and Cybernetics*, 39:1543–1555, 2009.

[84] J. G. Sled, A. P. Zijdenbos, and A. C. Evans. A nonparametric method for automatic correction of intensity nonuniformity in MRI data. *IEEE Trans. Med. Imaging*, 17:87–97, 1998.

[85] International consortium for brain mapping (ICBM). `http://www.loni.ucla.edu/ICBM/Downloads/Downloads_ICBMprobabilistic.shtml`.

[86] M. Jenkinson, P. R. Bannister, J. M. Brady, and S. M. Smith. Improved optimisation for the robust and accurate linear registration and motion correction of brain images. *NeuroImage*, 17:825–841, 2002.

[87] L. R. Dice. Measures of the amount of ecologic association between species. *Ecology*, 26:297–302, 1945.

[88] S. Valverde, A. Oliver, M. Cabezas, E. Roura, and X. Llado. Comparison of 10 brain tissue segmentation methods using revisited IBSR annotations. *Journal of Magnetic Resonance Imaging*, 1:93–101, 2014.

[89] T. G. Dietterich. Approximate statistical tests for comparing supervised classification learning algorithms. *Neural Computation*, 10:1895–1923, 1998.

[90] S. M. Smith. Fast robust automated segmentation. *Human Brain Mapping*, 17(3):143–155, 2002.

[91] N. Otsu. A threshold selection method from gray level histogram. *IEEE Transactions on Systems, Man, and Cybernetics*, 9:62–66, 1979.

[92] P. Soille. Morphological image analysis: Principles and applications. *Springer-Verlag*, 4(3):173–174, 1999.

[93] Y. Wen, L. He, K. M. von Deneen, and Y. Lu. Brain tissue classification based on DTI using an improved fuzzy c-means algorithm with spatial constraints. *Magnetic Resonance Imaging*, 31(9):1623–30, 2013.

[94] K. O. Babalola, B. Patenaude, P. Aljabar, J. Schnabel, D. Kennedy, W. Crum, S. Smith, T. F. Cootes, M. Jenkinson, and D. Rueckert. Comparison and evaluation of segmentation techniques for subcortical structures in brain MRI. *In Proceedings of Medical Image Computing and Computer Assisted Intervention (MICCAI)*, pages 409–416, 2008.

[95] IXI datasets. `http://www.brain-development.org`.

[96] Y. Shirvany. *Non-invasive EEG Functional Neuroimaging for Localizing Epileptic Brain Activity*. PhD thesis, Chalmers University of Technology, 2013.

[97] R. Grech, T. Cassar, J. Muscat, K. Camilleri, S. Fabri, M. Zervakis, P. Xanthopoulos, V. Sakkalis, and B. Vanrumste. Review on solving the inverse problem in EEG source analysis. *IEEE Transactions on Neural Systems and Rehabilitation Engineering*, 5(25), 2008.

[98] Y. Shirvany, A. R. Porras, K. Kowkabzadeh, Q. Mahmood, H. Lui, and M. Persson. Investigation of brain tissue segmentation error and its effect on EEG source localization. *In Proceedings of Engineering in Medicine and Biology Society (EMBC)*, pages 1522–25, 2012.

[99] C. H. Wolters, A. Anwander, X. Tricoche, D. Weinstein, M. A. Koch, and R. S. MacLeod. Influence of tissue conductivity anisotropy on EEG/MEG field and return current computation in a realistic head model: a simulation and visualization study using high-resolution finite element modeling. *NeuroImage*, 54:813–26, 2006.

[100] F. Edelvik, B. Andersson, S. Jakobsson, S. Larsson, M. Persson, and Y. Shirvany. An improved method for dipole modeling in EEG based source localization. *In Proceedings of International Federation for Medical and Biological Engineering (IFMBE)*, pages 146–149, 2009.

[101] K. Fassbender, C. Balucani, S. Walter, S. R. Levine, A. Haass, and J. Grotta. Streamlining of prehospital stroke management: the golden hour. *Lancet Neurol.*, 12:585–96, 2013.

[102] World Health Organization. `http://www.who.int/cardiovascular_diseases/resources/atlas/en/`.

[103] J. Chalela, C. S. Kidwell, L. M. Nentwich, M. Luby, J. A. Butman, A. M. Demchuk, M. D. Hill, N. Patronas, L. Latour, and S. Warach. Magnetic resonance imaging and computer tomography in emergency assessment of patients with suspected acute stroke: a prospective comparison. *The Lancet*, 369:293–298, 2007.

[104] T. Hölscher, J. V. Dunford, F. Schlachetzki, S. Boy, T. Hemmen, B. C. Meyer, J. Serra, J. Powers, and A. Voie. Prehospital stroke diagnosis and treatment in ambulances and helicopters-a concept paper. *Am. J. Emerg. Med.*, 31:743–7, 2013.

[105] S. Walter, P. Kostopoulos, A. Haass, I. Keller, M. Lesmeister, T. Schlechtriemen, C. Roth, P. Papanagiotou, I. Grunwald, H. Schumacher, and et al. Diagnosis and treatment of patients with stroke in a mobile stroke unit versus in hospital: a randomised controlled trial. *The Lancet Neurology*, 11:397–404, 2012.

[106] M. Persson, A. Fhager, H. Trefna, Y. Yu, T. McKelvey, G. Pegenius, J. E. Karlsson, and M. Elam. Microwave-based stroke diagnosis making global pre-hospital thrombolytic treatment possible. *IEEE Transactions on Biomedical Engineering*, 61:2806 – 2817, 2014.

[107] Tissue properties. `http://niremf.ifac.cnr.it/tissprop/`.

[108] A. Fhager. *Microwave tomography*. PhD thesis, Chalmers University of Technology, 2006.

[109] A. Fhager, P. Hashemzadeh, and M. Persson. Reconstruction quality and spectral content of an electromagnetic time-domain inversion algorithm. *IEEE Transactions on Biomedical Engineering*, 53:1594–1604, 2006.

[110] S. Y. Semenov, A. E. Bulyshev, A. Abubakar, V. G. Posukh, Y. E. Sizov, A. E. Souvorov, P. M. van den Berg, and T. C. Williams. Microwave tomographic imaging of the high dielectric-contrast objects using different image-reconstrcution approaches. *IEEE Transactions on Microwave Theory and Techniques*, 53(7):2284–2294, 2005.

[111] Q. Mahmood, A. Chodorowski, A. Mehnert, and M. Persson. A novel Bayesian approach to adaptive mean shift segmentation of brain images. *In Proceedings of IEEE International Conference on Computer Based Medical Systems (CBMS)*, pages 1–6, 2012.

[112] M. N. Ahmed, S. M. Yamany, N. Mohamed, A. A. Farag, and T. Moriarty. A modified fuzzy c-means algorithm for bias field estimation and segmentation of MRI data. *IEEE Trans. Med. Imaging*, 21(3):193–199, 2002.

[113] W. Jiahui, V. Clement, R. Ashley, G. Sylvain, O. Clementine, P. Emilie, D. Guangwei, H. Xuemei, G. Guido, and S. M. Andreas. Multi-atlas segmentation of subcortical brain structures via the autoseg software pipeline. *Frontiers in Neuroinformatics*, 8(7):1–7, 2014.